

4D-Explorer: A visual software for 4D-STEM data processing and image reconstruction

Yiming Hu^{*1}, Si Gao^{*1,2}, Xiaopeng Wu³, Xudong Pei¹, Futao Huang¹, Wei Mao¹, Weiyang Zhang¹, Aidan Horne³, Zhengbin Gu¹, and Peng Wang^{†1,3}

¹*National Laboratory of Solid State Microstructures, Jiangsu Key Laboratory of Artificial Functional Materials, College of Engineering and Applied Sciences and Collaborative Innovation Center of Advanced Microstructures, Nanjing University, Nanjing 210093, China.*

²*College of Materials Science and Engineering, Nanjing Tech University, Nanjing 210009, China.*

³*Department of Physics, University of Warwick, Coventry CV4 7AL, UK.*

June 12, 2023

Abstract

With the development of high-speed electron detectors, four-dimensional scanning transmission electron microscopy (4D-STEM) has emerged as a powerful tool for characterizing microstructures in material science and life science. However, the complexity of 4D-STEM data processing necessitates an intuitive graphical user interface software for researchers. In this regard, we have developed 4D-Explorer, an open-source, lightweight and extensible software for processing 4D-STEM data. It offers a visual and interactive workflow, including data preparation, calibration, image reconstruction and generating quantitative results. Furthermore, during calibration, our software includes a novel algorithm for rotational offset correction that uses a defocused 4D-STEM dataset and its axial bright field image, which has lower experimental requirements than conventional methods. We anticipate that 4D-Explorer will help researchers harness the capabilities of 4D-STEM technology.

Key Words: 4D-STEM, diffraction, open-source software, data processing

^{*}These authors contributed equally: Yiming Hu and Si Gao.

[†]Corresponding author: Peng Wang. Email address: peng.wang.3@warwick.ac.uk

1 Introduction

The state-of-the-art scanning transmission electron microscopes (STEM) have been widely used to image and characterize atom positions [1–3]. Recently, owing to the development of high-speed pixelated electron detectors [4–13], full diffraction images can be recorded in a short acquisition time. When the electron beam scans over the 2D real space (the sample plane), the fast detector records diffraction images in the 2D reciprocal space (the diffraction plane). These diffraction images make up the four-dimensional scanning transmission electron microscopy (4D-STEM) dataset [14], which contains rich information that can be retrieved to reveal local interaction details between the electron beam and the sample after the acquisition process.

4D-STEM is a powerful technique that offers a range of imaging modes for various applications including virtual imaging [15–23], positional averaged convergent beam electron diffraction (PACBED) [24, 25], differential phase contrast (DPC) [21, 26, 27], and electron ptychography [28–39]. These techniques can be used to generate orientation mapping [40–42], phase mapping [17, 18, 42] and strain mapping [43–50]. One rapidly developing technique is center of mass (CoM) imaging which has the same physical origin as DPC using segmented detectors [51, 52]. CoM images are phase contrast images that are sensitive to light elements, and can also characterize electrostatic [51] and magnetic fields of samples [53] with atomic-level precision. Meanwhile, the integrated CoM (iCoM) and differentiated CoM (dCoM) images can respectively provide information about the electrostatic potential and charge density of the sample [54].

Currently, there are various open-source software packages available for 4D-STEM data processing, such as py4DSTEM [55], LiberTEM [56], Pycroscopy [57], Nion Swift [58], riCOM [59] and PtychoSTEM [60]. However, due to the complexity of 4D-STEM data processing, there are still some challenges in software development. First, the size of 4D-STEM datasets ranges from several GBs to TBs, which may exceed the typical memory capacity of personal laptops. Second, the high dimensionality of the data makes it difficult to directly view and interactively calibrate. Third, different research fields may require flexible and customizable data processing methods due to the diversity of experimental environments and sample types.

To address these challenges, we have developed an open-source software, 4D-Explorer. The software supports major operating systems (Windows, MacOS, Linux) and can be run on weaker hardware such as personal laptops with satisfactory performance. With 4D-Explorer, we achieved a complete and interactive 4D-STEM data processing workflow, resulting in various imaging modes. In addition, we demonstrated the impact of rotational offset correction and diffraction alignment on CoM imaging. We proposed a novel method to find the rotational offset angle using the axial bright field (Axial BF) image of a defocused 4D-STEM dataset. Furthermore, during image reconstruction, 4D-Explorer can calculate and display contrast transfer functions in real-time to assist users in optimizing reconstruction parameters and interpreting results. Our experimental results validated the effectiveness of the calibration and image reconstruction algorithms, resulting in quantitative imaging.

2 Software Features

4D-Explorer, written in Python and utilizing open-source libraries from the scientific computation community, provides a visual framework for time-consuming data processing, including a file manager, a task manager, and several data viewers. Figure 1 is a screenshot of the main window of the software, and functions of the components are displayed in Supplementary Figure S4. Each component of the software addresses specific challenges in 4D-STEM data processing. The file manager and task manager handle the storage and computation of large datasets, while the data viewers provide flexible display options based on different purposes, processing methods and data dimensions.

File Manager The file manager organizes and stores data, including lines, images, vector fields, and 4D-STEM datasets, all within a single HDF5 [61] file, as shown in Supplementary Figure S7. It provides flexible data storage and high-performance input/output (IO), and loads data lazily to avoid memory overflow. The file manager handles different data types appropriately by distinguishing them through their respective file extensions, for example, “.4dstem” for 4D-STEM datasets, “.vec” for vector fields, and “.img” for 2D images. In addition, each data item in the file manager has its own set of attributes, which stores experimental parameters and other relevant information, as shown in Supplementary Figure S9. Users can view and edit the attributes as needed.

Task Manager The task manager in 4D-Explorer schedules time-consuming computation processes in the background, preventing the GUI from being unresponsive. The task manager uses a queue-style scheduling algorithm to avoid conflicts that may arise when different tasks modify the same dataset. Users can view the progress, status, details, error messages, and history of these tasks (See Supplementary Figure S6 III).

With both task manager and file manager, 4D-Explorer offers a 4D-STEM data processing with acceptable performance on handling big data using personal laptops. The time consumed by data loading and processing depends on the IO speed of the storage devices. For a 4 GB 4D-STEM dataset stored in a hard disk drive (HDD), it costs 48 s for image reconstruction and 127 s for calibration, which depend on the reading speed and writing speed of the disk respectively. However, if the dataset is stored in a solid state drive (SSD), the time is reduced to 17 s and 21 s for reconstruction and calibration respectively. As the disk input/output (IO) becomes the limiting factor, the CPU utilization remains below 10%, and the memory usage is kept below 130 MB. Generally, the time consumption scales linearly with the size of the dataset.

Viewer A viewer in 4D-Explorer is a page designed to display different types of data according to their specific display requirements and purposes. Each viewer embeds Matplotlib windows [62] for interactive, multiplatform, and high-quality visualization. There are currently three types of base viewers: image viewer, vector field viewer, and 4D-STEM viewer. The image viewer allows us to adjust display effects such as brightness, contrast, and interpolation algorithms, as well as pan and zoom-in on displaying regions and view its histogram (Supplementary Figure S11). The vector field viewer displays quiver plots with a background image that visually demonstrates the distribution of electric fields at the atomic level along with their potential or charge density

(Supplementary Figure S12). Meanwhile, the 4D-STEM viewer can simultaneously display diffraction patterns and a preview image (Figure 1). By interactively dragging the cursor on the preview image, we can explore different diffraction patterns. This preview image’s correspondence with the diffraction patterns facilitates an intuitive understanding of the 4D-STEM dataset and potential problem diagnosis.

Extensibility The architecture and the python open-source scientific computing ecosystem provide the functional extensibility of 4D-Explorer. Users are able to handle the HDF5 dataset directly by many other open-source tools when they need advanced processing. Among these tools, LiberTEM [56] provides graphic interfaces based on Jupyter notebook and parallel imaging algorithms following the Map-Reduce model, but currently lacks visual calibration functions. Therefore, we can first use 4D-Explorer to calibrate 4D-STEM datasets and then use LiberTEM for parallel reconstruction, especially in the cases where the process becomes computationally intensive. Other software packages such as pyXem [63] and Pycroscopy [57] contain comprehensive calibration and reconstruction algorithms, but they are limited in the aspect of graphical interface. As a complementation, 4D-Explorer provides convenient methods for primary analysis that help users to quickly detect imaging defects and select customized calibration algorithms. Moreover, The GUI and file manager also provide an opportunity for users to implement customized algorithm and method development without concern for data display and IO issues.

Overall, 4D-Explorer is designed with both usability and flexibility in mind. With the help of the file manager, task manager, and various viewers, this tool can significantly lower the barriers for researchers from different fields who wish to explore the world of 4D-STEM techniques and quickly obtain results.

3 Workflow

The workflow of 4D-STEM dataset processing typically involves four major steps: preparation, calibration, reconstruction, and output generation, as illustrated in Figure 2. In this section, we demonstrate the calibration step using a gold nanoparticle-modified DNA sample, and high-resolution image reconstruction step using a monolayer MoS₂ sample. The 4D-STEM experiments are performed using an aberration-corrected FEI Titan³ Cubed 60-300 STEM equipped with an electron microscopy pixel arrayed detector (EMPAD). The experimental parameters used for the acquisition are listed in Table 1.

3.1 Preparation

To begin with the preparation step, we first create a new HDF5 file. Then, the raw 4D-STEM datasets can be imported into the HDF5 file via the file manager. Currently, the software can automatically import RAW files from EMPAD [6] and MIB files from Merlin Medipix3 [4] (Supplementary Figure S10). The experimental parameters of the 4D-STEM dataset, such as accelerating voltage U , convergent semi-angle α , camera length (CL), and scanning step size, can be automatically parsed and stored as attributes of the dataset (Supplementary Figure S9). These experimental parameters can also be manually edited and will be useful in later steps of the workflow.

3.2 Calibration

Calibration is an essential step to acquire accurate and meaningful 4D-STEM data. It is not uncommon for the instrument to be not well calibrated, which can lead to inaccuracies in the calculated parameters. To obtain quantified 4D-STEM results, neither of the two calibration procedures, rotational offset correction and diffraction alignment, can be neglected. In addition to these two procedures, 4D-Explorer also provides user-friendly interfaces for other calibration options, such as background subtraction (Supplementary Figure S13). Further development and implementation of calibration algorithms and methods will continue to be explored to improve the accuracy and reliability of 4D-STEM results.

Rotational Offset Correction The rotational offset in electron microscopes, which refers to the rotation between the scanning coordinate and the detector coordinate, arises from three sources shown in Supplementary Figure S2. Firstly, the helical trajectory of electrons caused by magnetic lenses induces a rotation in the electron beam, which in turn causes a rotation in the formed image [64]. Secondly, different choices of coordinate basis during computing, such as using $x - y$ coordinates versus $i - j$ indices, can lead to an additional rotation. Lastly, manually set scanning rotations in the experiment also contribute to the overall rotational offset. These three angles from the sources can be summarized as θ , as shown in Figure 3a. Although the rotational offset does not affect virtual imaging, its correction is essential for modes that are determined by the orientations of diffraction patterns, such as strain mapping, orientation mapping, DPC and CoM. To measure the rotational offset, 4D-Explorer provides following two methods.

The first method to measure the rotational offset angle is to compare the sample features between the real-space scanning image and the shadow image, which contains the sample shape information in the diffraction patterns. In a conventional approach of this method [55], the real-space scanning image can be an in-focus STEM image, while the shadow image is acquired from a defocused diffraction image. Here we propose a novel approach that replaces the in-focus STEM image with the Axial BF image reconstructed from a defocused 4D-STEM dataset. The Axial BF image is a good approximation of the conventional TEM (CTEM) image due to the reciprocity theory [65], and thus it has a large depth of fields. Therefore, it can preserve the sample features when the defocus is as large as about $2\ \mu\text{m}$ in our experiment. Compared to the conventional approach, our approach only requires one single defocused 4D-STEM dataset, which simplifies the experimental operation and avoids the challenge of drifting that may arise during changes in defocus values. However, it should be noted that the shadow image of underfocus and overfocus datasets may be rotated 180° with respect to each other. Moreover, the sample features in the shadow images may be distorted by a large aberration, which could lead to an error in the measurement of θ .

The second method is to compute the curl of the CoM (Supplementary Figure S14). This method can be used when a defocused pairing dataset for calibration is not accessible, as it only requires the experimental 4D-STEM dataset itself. When the thin phase object approximation holds, we can obtain the CoM field distribution of the sample. The CoM field should be irrotational, since it is proportional to the gradient

of the projected electric potential [54]:

$$\mathbf{I}_{\text{CoM}}(\mathbf{r}_p) = \frac{1}{2\pi} [|\psi_{\text{in}}(\mathbf{r})|^2 \star \nabla\phi(\mathbf{r})](\mathbf{r}_p) \quad (1)$$

where ψ_{in} is the wave function of electron probe, ϕ is the modulating phase-change function of the sample, \mathbf{r} is a pseudo-variable denoting locations of the sample, and \mathbf{r}_p denotes the positions on the scanning plane. The \star operator denotes cross-correlation¹ here. Note that ϕ is actually proportional to the projected electric potential of the sample. Then the angle can be determined by rotating each CoM vector and minimizing the sum of the squared curl:

$$\theta = \arg \min_{\theta} \int_{\mathbb{R}^2} |\nabla_p \times \mathbf{I}_{\text{CoM}}(\mathbf{r}_p; \theta)|^2 d^2\mathbf{r}_p \quad (2)$$

where $\nabla_p \times$ is the curl operator in the offset coordinate. The theory of the CoM-based method can be found in Supplementary Information 5. A similar method is also mentioned in [55], and it has the same physical origin as the J-Matrix method introduced by [66].

In Figure 3, we present the process of rotational offset correction using the two methods. In the first method, the axial BF in Figure 3c is sharp and clear enough for matching features to the diffraction pattern in Figure 3b and resulting in 25° as the rotational offset angle, while the conventional ABF and ADF images appear blurred as shown in Supplementary Figure S1. We note that for underfocused datasets, the diffraction image will be rotated an additional 180°, as evidenced in Figure 3b, where the white arrow is rotated 205° compared to the arrow in Figure 3c. In the second method, on the other hand, we use the curl of the CoM field to determine the optimal rotational offset angle. The curl of CoM reaches minimum at an angle of 24.8° in Figure 3f, coinciding with the result from the first method. The iCoM images before and after the correction are shown in Figure 3g and Figure 3h, while Figure 3d and Figure 3e correspond to the CoM fields in the region of the white square in Figure 3g and Figure 3h, respectively. After the correction, the vector arrows of CoM in Figure 3e point towards the centers of gold nanoparticles, consistent with our expectation. However, there are still artifacts in the iCoM image Figure 3h after the correction, which will be eliminated by further diffraction alignment.

Diffraction Alignment Diffraction alignment plays an important role in the accuracy of CoM images by moving the optical axis to the center of the diffraction images. The CoM of each diffraction pattern can be offset from the digital center due to various reasons, including the sample electric field scattering the electron beam, optical axis misalignment, and scanning induced diffraction wobble [67]. To obtain a precise electric field distribution of the sample, it is necessary to reduce the impact of the latter two factors. Notably, the problem of diffraction wobble becomes critical when the scanning field of view exceeds tens of nanometers and may result in artifacts in the CoM results [55].

For the misalignment of the optical axis, 4D-Explorer provides a visualization window to manually adjust the position of the bright field diffraction disk, so that it can

¹Cross correlation is defined as for $f(\mathbf{r})$ and $g(\mathbf{r})$, $[f(\mathbf{r}) \star g(\mathbf{r})](\mathbf{r}') = \int_{\mathbb{R}^2} f^*(\mathbf{r})g(\mathbf{r}' + \mathbf{r})d^2\mathbf{r}$.

be shifted to the center of the image, as shown in Supplementary Figure S15. Subsequently, the measured shift value can be applied to all diffraction patterns in the 4D-STEM dataset to accomplish the diffraction alignment.

Diffraction wobble, however, results in varying displacements of the bright field diffraction disks relative to the center of each image, and thus each diffraction image requires individual measurements. In 4D-Explorer, two methods are available for measuring the displacements. The first method is to acquire a reference 4D-STEM dataset without the sample under the same experimental conditions, and calculating its CoM vector distribution. This CoM vector distribution is then applied as the translation vectors to align the experimental dataset with the sample.

The second method to address the diffraction wobble issue is fitting, when no reference dataset is recorded in the experiment. We can select scanning points where there are no sample structures, and locate the center of the bright field diffraction disk. Then, we fit a linear or polynomial function through the displacement of the selected points to determine the translation vectors. In Figure 4, we present the result of CoM reconstruction before and after the alignment process. The input dataset used for this process is the outcome of the rotational offset correction we mentioned earlier. Prior to alignment, the presence of diffraction wobble in the dataset result in large-scale contrast artifacts in the iCoM image Figure 4a, which also contribute to the background vectors in Figure 4b. Additionally, in Figure 4c, we can observe that the locations of the bright field diffraction disk at the ends of the dashed line in Figure 4a do not coincide. In Figure 4g, we draw the distributions of the x and y components of CoM vectors and their corresponding fit functions along this dashed line. After applying the translation to each diffraction image, the artifacts in the iCoM image are eliminated in Figure 4d, the background vectors in Figure 4e are subtracted, and the diffraction disks are aligned and registered in Figure 4f.

In summary, the calibration process employed in 4D-Explorer involves multiple steps and methods, such as rotational offset correction and diffraction alignment, to ensure high-quality 4D-STEM imaging, particularly CoM imaging. Throughout the calibration process, the CoM fields of the gold nanoparticles modified DNA evolve from Figure 3d to Figure 3e, and then from Figure 4b to Figure 4e, ultimately resulting in a clear electrostatic field image of the sample. In parallel, the iCoM images of the sample also undergo a transformation from Figure 3g to Figure 3h, and then from Figure 4a to Figure 4d, resulting in a phase contrast image of both gold nanoparticles and DNA molecules.

3.3 Reconstruction

With the rich information provided by 4D-STEM datasets, specific reconstruction methods are required to generate and interpret images. These methods are necessary to extract the full potential of the data and provide a comprehensive understanding of the sample. The 4D-Explorer software currently offers two reconstruction modes: virtual imaging and center of mass. However, more algorithms are planned for future releases to further enhance the capabilities of 4D-STEM imaging.

Virtual Imaging To generate virtual images, different regions of interest (ROIs) can be selected as virtual detectors on the diffraction patterns. The signals from the diffraction patterns within each ROI are then integrated and mapped onto the scanning

coordinate system to form a virtual imaging result. The properties of virtual imaging modes are consistent with those of conventional STEM images when the virtual detector and conventional STEM detector have the same collection angle. In Figure 5, there are some common virtual imaging modes include bright field (BF), annular bright field (ABF) and annular dark field (ADF) of MoS₂ sample. In addition to these modes, Axial BF, middle angle bright field (MaBF) [68] and enhanced annular bright field (eABF) [68] can also be calculated. These modes provide additional flexibility in generating virtual images and can be used to extract specific information from the 4D-STEM dataset.

Center of Mass The distribution of the CoM vector field is obtained by computing the center of mass of each diffraction pattern, which reveals the momentum transfer of the electron beam caused by internal electric fields in the sample. For thin, non-magnetic samples, the CoM vector field is proportional to the projected local electric field. As the potential of the CoM field, integrated CoM (iCoM) is proportional to the projected electric potential. On the other hand, as the divergence of CoM vector field, differentiated CoM (dCoM) is proportional to the projected charge density according to Maxwell’s Theorem. Figure 6 shows atomic-resolution CoM reconstructions of the MoS₂ sample. Figure 6a and Figure 6b show dCoM and iCoM reconstructions, respectively, while Figure 6c displays the distribution of projected electric field with projected charge density as background.

Contrast Transfer Functions The contrast of imaging modes depends on experimental parameters and can be explained using the contrast transfer functions (CTF). The 4D-Explorer software provides a real-time calculation of the CTF for different virtual imaging modes, which can guide users in selecting reconstruction parameters and interpreting the results. Figure 7 shows the analytical results of the CTF for various modes.

The calculations of CTFs of virtual imaging follows [69] and can be found in Supplementary Information 2. Figure 7a displays the CTF for Axial BF, which is consistent with the one of the reverse-path TEM, as mentioned in the rotational offset correction of the calibration step. The transfer function of TEM is truncated at the spatial frequency corresponding to the radius of the bright-field diffraction disk, because we use the radius of the convergence aperture in STEM as the objective aperture radius in TEM. Figure 7b shows the CTF for ABF, which exhibits an inverted contrast as defocus changes sign, indicating its sensitivity to imaging conditions. Figure 7c shows the CTF for eABF, which is the difference between ABF and MaBF. eABF has an enhanced contrast, as ABF and MaBF have opposite contrasts at the same defocus, which can also be observed in Figure 5b and Figure 5c. Figure 7d displays the bright field image using a virtual detector covering the full bright field disk (Full BF) and ADF. Note that Full BF and ADF do not have a contrast transfer under weak phase object approximation (WPOA), so their CTFs are calculated against $1 - \cos \phi \approx \frac{1}{2}\phi^2$, where ϕ is the phase-change function of the sample. This also means that Full BF and ADF have lower contrast for light element samples. Unlike ABF, however, Full BF and ADF do not exhibit a contrast inversion with changing defocus sign, resulting in more stable imaging.

The calculation of the CTFs for the Center of Mass imaging mode is based on [54] and can be found in Supplementary Information 4. Figure 7e displays the CTF of

dCoM with different defocus values. Due to the differential operations involved in the calculation of dCoM, the CTF curve of dCoM exhibits large absolute values. Figure 7f shows the CTF of iCoM. Although the shape of the CTF curve of iCoM is similar to that of ADF, the CTF of iCoM is based on ϕ rather than ϕ^2 , making it better suited for imaging light-element samples than ADF. Compared to the CTF of ABF, the CTF of iCoM does not exhibit contrast reversal at different defocus values, resulting in better interpretability of iCoM images.

3.4 Output Generation

The reconstruction results, as data matrices, are stored in the same HDF5 file along with the original 4D-STEM dataset, and can be exported in multiple data formats. Advanced analysis that is customized to a specific dataset can then be performed with other 4D-STEM softwares. For visualization, the image and vector field results can be rendered and viewed directly in 4D-Explorer through different viewers, and they can also be exported as high-quality plots to many image file formats.

4 Conclusion

In this paper, we have introduced 4D-Explorer, an open-source software tool designed for 4D-STEM data processing and analysis. The software provides a complete visual workflow for data processing. For calibration, it integrates rotational offset correction and diffraction alignment. We have proposed a novel method for finding the rotational offset angle using the Axial BF image of a defocused 4D-STEM dataset. This approach has been experimentally validated and shown to be effective in achieving high-quality imaging results. For image reconstruction, 4D-Explorer includes virtual imaging and CoM that can reveal rich information about the sample. It also integrates real-time calculation and display of the transfer function during image reconstruction, which facilitates the selection of optimal reconstruction parameters and interpretation of reconstruction results. Overall, the software is user-friendly, cross-platform and extensible, making itself a valuable tool for researchers of various fields using 4D-STEM techniques.

In future, there are several potential avenues for further development of 4D-Explorer software. One direction is the integration of machine learning algorithms to automate and optimize data processing workflows. This could include automated calibration, as well as more advanced image reconstruction techniques that leverage the power of deep learning [70]. Another area for future development is the incorporation of additional imaging modes. For example, in low-dose 4D-STEM experiment, using event-driven detectors [12, 71] to produce sparse datasets can effectively reduce the dataset size and acquiring duration, and thus the sparse datasets processing could be supported by 4D-Explorer. Additionally, combining 4D-STEM with other imaging techniques such as electron energy loss spectroscopy (EELS) could enable even more comprehensive characterization of materials [33].

Users can visit [our website](#) for standalone executable applications, tutorials, documents and example datasets. The source codes are available in the [Github repository](#). Users and developers are welcome to try our software and provide us with opinions, suggestions and contributions.

Acknowledgements

The authors would like to acknowledge funding from the National Natural Science Foundation of China (11874199, 21991134, 21934007, 92056117), University of Warwick Research Development Fund (RDF) 2021-22 Science Development Award, Natural Science Foundation of Jiangsu Province (BK20210187) and China Postdoctoral Science Foundation (No. 2022M711564). The authors thank Weina Fang for the preparation of the Gold Nanoparticle-modified DNA sample.

References

- [1] Philip E. Batson, Niklas Dellby, and Ondrej L. Krivanek. Sub-ångstrom resolution using aberration corrected electron optics. *Nature*, 418(6898):617–620, 2002.
- [2] Peter D. Nellist, Matthew F. Chisholm, N. Dellby, O. L. Krivanek, M. F. Murfitt, Z. S. Szilagy, Andrew R. Lupini, A. Borisevich, W. H. Sides Jr., and S. J. Pennycook. Direct sub-Ångstrom imaging of a crystal lattice. *Science*, 305(5691):1741, 2004.
- [3] O. L. Krivanek, P. D. Nellist, N. Dellby, M. F. Murfitt, and Z. Szilagy. Towards sub-0.5 Å electron beams. *Ultramicroscopy*, 96(3-4):229–237, 2003.
- [4] R. Plackett, I. Horswell, E. N. Gimenez, J. Marchal, D. Omar, and N. Tartoni. Merlin: A fast versatile readout system for Medipix3. *Journal of Instrumentation*, 8(01):C01038, 2013.
- [5] H. Yang, L. Jones, H. Ryll, M. Simson, H. Soltau, Y. Kondo, R. Sagawa, H. Banba, I. Maclaren, and P. D. Nellist. 4D STEM: High efficiency phase contrast imaging using a fast pixelated detector. *Journal of Physics: Conference Series*, 644:012032, 2015.
- [6] Mark W. Tate, Prafull Purohit, Darol Chamberlain, Kayla X. Nguyen, Robert Hovden, Celesta S. Chang, Pratiti Deb, Emrah Turgut, John T. Heron, Darrell G. Schlom, Daniel C. Ralph, Gregory D. Fuchs, Katherine S. Shanks, Hugh T. Philipp, David A. Muller, and Sol M. Gruner. High dynamic range pixel array detector for scanning transmission electron microscopy. *Microscopy and Microanalysis*, 22(1):237–249, 2016.
- [7] Jim Ciston, Ian J. Johnson, Brent R. Draney, Peter Ercius, Erin Fong, Azriel Goldschmidt, John M. Joseph, Jason R. Lee, Alexander Mueller, Colin Ophus, Ashwin Selvarajan, David E. Skinner, Thorsten Stezelberger, Craig S. Tindall, Andrew M. Minor, and Peter Denes. The 4D camera: Very high speed electron counting for 4D-STEM. *Microscopy and Microanalysis*, 25(S2):1930–1931, 2019.
- [8] Peter Ercius, Ian Johnson, Hamish Brown, Philipp Pelz, Shang-Lin Hsu, Brent Draney, Erin Fong, Azriel Goldschmidt, John Joseph, Jason Lee, Jim Ciston, Colin Ophus, Mary Scott, Ashwin Selvarajan, David Paul, David Skinner, Marcus Hanwell, Chris Harris, Patrick Avery, Thorsten Stezelberger, Craig Tindall, Ramamoorthy Ramesh, Andrew Minor, and Peter Denes. The 4D camera – an

- 87 kHz frame-rate detector for counted 4D-STEM experiments. *Microscopy and Microanalysis*, 26(S2):1896–1897, 2020.
- [9] Barnaby D.A. Levin, Chenyu Zhang, Benjamin Bammes, Paul M. Voyles, and Robert B. Bilhorn. 4D STEM with a direct electron detector. *Microscopy and Analysis*, 34:20–22, 2020.
- [10] Benedikt Haas, Andreas Mittelberger, Chris Meyer, Benjamin Plotkin-Swing, Niklas Dellby, Ondrej Krivanek, Tracy Lovejoy, and Christoph Koch. High-fidelity 4D-STEM enabled by live processing at 15'000 detector frames per second. *Microscopy and Microanalysis*, 27(S1):994–997, 2021.
- [11] Debaditya Chatterjee, Jingrui Wei, Alex Kvit, Benjamin Bammes, Barnaby Levin, Robert Bilhorn, and Paul Voyles. An ultrafast direct electron camera for 4D STEM. *Microscopy and Microanalysis*, 27(S1):1004–1006, 2021.
- [12] Daen Jannis, Christoph Hofer, Chuang Gao, Xiaobin Xie, Armand Béch e, Timothy J. Pennycook, and Jo Verbeeck. Event driven 4D STEM acquisition with a Timepix3 detector: Microsecond dwell time and faster scans for high precision and low dose applications. *Ultramicroscopy*, 233:113423, 2022.
- [13] P. Zambon, S. Bottinelli, R. Schnyder, D. Musarra, D. Boye, A. Dudina, N. Lehmann, S. De Carlo, M. Rissi, C. Schulze-Briese, M. Meffert, M. Campanini, R. Erni, and L. Piazza. KITE: High frame rate, high count rate pixelated electron counting ASIC for 4D STEM applications featuring high-Z sensor. *Nuclear Instruments and Methods in Physics Research Section A: Accelerators, Spectrometers, Detectors and Associated Equipment*, 1048:167888, 2023.
- [14] Colin Ophus. Four-dimensional scanning transmission electron microscopy (4D-STEM): From scanning nanodiffraction to ptychography and beyond. *Microscopy and Microanalysis*, 25(3):563–582, 2019.
- [15] J. J. Funderberger, A. Morawiec, Emmanuel Bouzy, and Jean-S ebastien Lecomte. Polycrystal orientation maps from TEM. *Ultramicroscopy*, 96(2):127–137, 2003.
- [16] M. Watanabe and D. B. Williams. Development of diffraction imaging for orientation analysis of grains in scanning transmission electron microscopy. *Microscopy and Microanalysis*, 13(S02):962–963, 2007.
- [17] Thomas A. Caswell, Peter Ercius, Mark W. Tate, Alper Ercan, Sol M. Gruner, and David A. Muller. A high-speed area detector for novel imaging techniques in a scanning transmission electron microscope. *Ultramicroscopy*, 109(4):304–311, 2009.
- [18] Christoph Gammer, V. Burak Ozdol, Christian H. Liebscher, and Andrew M. Minor. Diffraction contrast imaging using virtual apertures. *Ultramicroscopy*, 155:1–10, 2015.
- [19] Andrew R. Lupini, Miaofang Chi, Sergei V. Kalinin, Albina Y. Borisevich, Juan Carlos Idrobo, and Stephen Jesse. Ptychographic imaging in an aberration corrected stem. *Microscopy and Microanalysis*, 21(S3):1219–1220, 2015.

- [20] Colin Ophus, Jim Ciston, Jordan Pierce, Tyler R. Harvey, Jordan Chess, Benjamin J. McMorran, Cory Czarnik, Harald H. Rose, and Peter Ercius. Efficient linear phase contrast in scanning transmission electron microscopy with matched illumination and detector interferometry. *Nature Communications*, 7:10719, 2016.
- [21] Jordan A. Hachtel, Juan Carlos Idrobo, and Miaofang Chi. Sub-Ångstrom electric field measurements on a universal detector in a scanning transmission electron microscope. *Advanced Structural and Chemical Imaging*, 4(1):10, 2018.
- [22] Shamail Ahmed, Matteo Bianchini, Anuj Pokle, Manveer Singh Munde, Pascal Hartmann, Torsten Brezesinski, Andreas Beyer, Jürgen Janek, and Kerstin Volz. Visualization of light elements using 4D STEM: the layered-to-rock salt phase transition in LiNiO₂ cathode material. *Advanced Energy Materials*, 10(25):2001026, 2020.
- [23] Elisabeth Thronsen, Jonas Frafjord, Jesper Friis, Calin Daniel Marioara, Sigurd Wenner, Sigmund Jarle Andersen, and Randi Holmestad. Studying GPI zones in Al-Zn-Mg alloys by 4D-STEM. *Materials Characterization*, 185:111675, 2022.
- [24] James M. LeBeau, Scott D. Findlay, Leslie J. Allen, and Susanne Stemmer. Position averaged convergent beam electron diffraction: Theory and applications. *Ultramicroscopy*, 110:118–125, 2010.
- [25] James A. Pollock, Matthew Weyland, D. J. Taplin, L. J. Allen, and S. D. Findlay. Accuracy and precision of thickness determination from position-averaged convergent beam electron diffraction patterns using a single-parameter metric. *Ultramicroscopy*, 181:86–96, 2017.
- [26] H. Rose. Phase contrast in scanning transmission electron microscopy. *Optik*, 39(4):416–436, 1974.
- [27] N. H. Dekkers and H. de Lang. Differential phase contrast in a STEM. *Optik*, 41(4):452–456, 1974.
- [28] W. Hoppe. Diffraction in inhomogeneous primary wave fields 1. principle of phase determination from electron diffraction interference. *Acta Crystallographica Section A: Crystal Physics Diffraction Theoretical and General Crystallography*, 25:495–501, 1969.
- [29] J. M. Rodenburg and R. H. T. Bates. The theory of super-resolution electron microscopy via Wigner-distribution deconvolution. *Philosophical Transactions of the Royal Society of London. Series A: Physical and Engineering Sciences*, 339(1655):521–553, 1992.
- [30] P. D. Nellist, B. C. McCallum, and John M. Rodenburg. Resolution beyond the ‘information limit’ in transmission electron microscopy. *Nature*, 374(6523):630–632, 1995.
- [31] Peng Wang, Fucui Zhang, Si Gao, Mian Zhang, and Angus I. Kirkland. Electron ptychographic diffractive imaging of boron atoms in LaB₆ crystals. *Scientific Reports*, 7(1):2857, 2017.

- [32] Si Gao, Peng Wang, Fucai Zhang, Gerardo T Martinez, Peter D. Nellist, Xiaoqing Pan, and Angus I. Kirkland. Electron ptychographic microscopy for three-dimensional imaging. *Nature Communications*, 8:163, 2017.
- [33] Biying Song, Zhiyuan Ding, Christopher S. Allen, Hidetaka Sawada, Fucai Zhang, Xiaoqing Pan, Jamie Warner, Angus I. Kirkland, and Peng Wang. Hollow electron ptychographic diffractive imaging. *Physical Review Letters*, 121(14):146101, 2018.
- [34] Yi Jiang, Zhen Chen, Yimo Han, Pratiti Deb, Hui Gao, Saien Xie, Prafull Purohit, Mark W. Tate, Jiwoong Park, Sol M. Gruner, Veit Elser, and David A. Muller. Electron ptychography of 2D materials to deep sub-ångström resolution. *Nature*, 559(7714):343–349, 2018.
- [35] Jiamei Song, Christopher S. Allen, Si Gao, Chen Huang, Hidetaka Sawada, Xiaoqing Pan, Jamie Warner, Peng Wang, and Angus I. Kirkland. Atomic resolution defocused electron ptychography at low dose with a fast, direct electron detector. *Scientific Reports*, 9:3919, 2019.
- [36] Zhen Chen, Michal Odstrcil, Yi Jiang, Yimo Han, Ming-Hui Chiu, Lain-Jong Li, and David A. Muller. Mixed-state electron ptychography enables sub-angstrom resolution imaging with picometer precision at low dose. *Nature Communications*, 11:2994, 2020.
- [37] Liqi Zhou, Jingdong Song, Judy S. Kim, Xudong Pei, Chen Huang, Mark Boyce, Luiza Mendonça, Daniel Clare, Alistair Siebert, Christopher S. Allen, Emanuela Liberti, David I. Stuart, Xiaoqing Pan, Peter D. Nellist, Peijun Zhang, Angus I. Kirkland, and Peng Wang. Low-dose phase retrieval of biological specimens using cryo-electron ptychography. *Nature Communications*, 11:2773, 2020.
- [38] Zhen Chen, Yi Jiang, Yu-Tsun Shao, Megan E. Holtz, Michal Odstrčil, Manuel Guizar-Sicairos, Isabelle Hanke, Steffen Ganschow, Darrell G. Schlom, and David A. Muller. Electron ptychography achieves atomic-resolution limits set by lattice vibrations. *Science*, 372(6544):826–831, 2021.
- [39] Xudong Pei, Liqi Zhou, Chen Huang, Mark Boyce, Judy S. Kim, Emanuela Liberti, Yiming Hu, Takeo Sasaki, Peter D. Nellist, Peijun Zhang, David I. Stuart, Angus I. Kirkland, and Peng Wang. Cryogenic electron ptychographic single particle analysis with wide bandwidth information transfer. *Nature Communications*, 14:3027, 2023.
- [40] Ouliana Panova, X. Chelsea Chen, Karen C. Bustillo, Colin Ophus, Mahesh P. Bhatt, Nitash Balsara, and Andrew M. Minor. Orientation mapping of semicrystalline polymers using scanning electron nanobeam diffraction. *Micron*, 88:30–36, 2016.
- [41] Jonas Kristoffer Sunde, Calin Daniel Marioara, Antonius T. J. van Helvoort, and Randi Holmestad. The evolution of precipitate crystal structures in an Al-Mg-Si (-Cu) alloy studied by a combined HAADF-STEM and SPED approach. *Materials Characterization*, 142:458–469, 2018.

- [42] Marcus Gallagher-Jones, Colin Ophus, Karen C. Bustillo, David R. Boyer, Ouliana Panova, Calina Glynn, Chih-Te Zee, Jim Ciston, Kevin Canton Mancina, Andrew M. Minor, and Jose A. Rodriguez. Nanoscale mosaicity revealed in peptide microcrystals by scanning electron nanodiffraction. *Communications Biology*, 2:26, 2019.
- [43] Koji Usuda, Tomohisa Mizuno, Tsutomu Tezuka, Naoharu Sugiyama, Yoshihiko Moriyama, Shu Nakaharai, and Shin-ichi Takagi. Strain relaxation of strained-Si layers on SiGe-on-insulator (SGOI) structures after mesa isolation. *Applied Surface Science*, 224(1-4):113–116, 2004.
- [44] Knut Müller, Andreas Rosenauer, Marco Schowalter, Josef Zweck, Rafael Fritz, and Kerstin Volz. Strain measurement in semiconductor heterostructures by scanning transmission electron microscopy. *Microscopy and Microanalysis*, 18(5):995–1009, 2012.
- [45] V. B. Ozdol, C. Gammer, X. G. Jin, P. Ercius, C. Ophus, J. Ciston, and A. M. Minor. Strain mapping at nanometer resolution using advanced nano-beam electron diffraction. *Applied Physics Letters*, 106(25):253107, 2015.
- [46] Benedikt Haas, Candice Thomas, Pierre-Henri Jouneau, Nicolas Bernier, Tristan Meunier, Philippe Ballet, and Jean-Luc Rouvière. High precision strain mapping of topological insulator HgTe/CdTe. *Applied Physics Letters*, 110(26):263102, 2017.
- [47] Thomas C. Pekin, Christoph Gammer, Jim Ciston, Andrew M. Minor, and Colin Ophus. Optimizing disk registration algorithms for nanobeam electron diffraction strain mapping. *Ultramicroscopy*, 176:170–176, 2017.
- [48] Thomas C. Pekin, Christoph Gammer, Jim Ciston, Colin Ophus, and Andrew M. Minor. In situ nanobeam electron diffraction strain mapping of planar slip in stainless steel. *Scripta Materialia*, 146:87–90, 2018.
- [49] Yimo Han, Kayla Nguyen, Michael Cao, Paul Cueva, Saien Xie, Mark W. Tate, Prafull Purohit, Sol M. Gruner, Jiwoong Park, and David A. Muller. Strain mapping of two-dimensional heterostructures with subpicometer precision. *Nano Letters*, 18(6):3746–3751, 2018.
- [50] Christoph Gammer, Colin Ophus, Thomas C. Pekin, Jürgen Eckert, and Andrew M. Minor. Local nanoscale strain mapping of a metallic glass during in situ testing. *Applied Physics Letters*, 112(17):171905, 2018.
- [51] Knut Müller, Florian F. Krause, Armand Béché, Marco Schowalter, Vincent Galioit, Stefan Löffler, Johan Verbeeck, Josef Zweck, Peter Schattschneider, and Andreas Rosenauer. Atomic electric fields revealed by a quantum mechanical approach to electron picodiffraction. *Nature Communications*, 5:5653, 2014.
- [52] Wenpei Gao, Christopher Addiego, Hui Wang, Xingxu Yan, Yusheng Hou, Dianxiang Ji, Colin Heikes, Yi Zhang, Linze Li, Huaixun Huyan, et al. Real-space charge-density imaging with sub-ångström resolution by four-dimensional electron microscopy. *Nature*, 575(7783):480–484, 2019.

- [53] Yuji Kohno, Takehito Seki, Scott D. Findlay, Yuichi Ikuhara, and Naoya Shibata. Real-space visualization of intrinsic magnetic fields of an antiferromagnet. *Nature*, 602(7896):234–239, 2022.
- [54] Ivan Lazić, Eric G.T. Bosch, and Sorin Lazar. Phase contrast STEM for thin samples: Integrated differential phase contrast. *Ultramicroscopy*, 160:265–280, 2016.
- [55] Benjamin H. Savitzky, Steven E. Zeltmann, Lauren A. Hughes, Hamish G. Brown, Shiteng Zhao, Philipp M. Pelz, Thomas C. Pekin, Edward S. Barnard, Jennifer Donohue, Luis Rangel DaCosta, Ellis Kennedy, Yujun Xie, Matthew T. Janish, Matthew M. Schneider, Patrick Herring, Chirranjeevi Gopal, Abraham Anapolsky, Rohan Dhall, Karen C. Bustillo, Peter Ercius, Mary C. Scott, Jim Ciston, Andrew M. Minor, and Colin Ophus. py4DSTEM: A software package for four-dimensional scanning transmission electron microscopy data analysis. *Microscopy and Microanalysis*, 27(4):712–743, 2021.
- [56] Alexander Clausen, Dieter Weber, Karina Ruzaeva, Vadim Migunov, Anand Baburajan, Abijith Bahuleyan, Jan Caron, Rahul Chandra, Sayandip Halder, Magnus Nord, Knut Müller-Caspary, and Rafal E. Dunin-Borkowski. LiberTEM: Software platform for scalable multidimensional data processing in transmission electron microscopy. *Journal of Open Source Software*, 5(50):2006, 2020.
- [57] Suhas Somnath, Chris R. Smith, Nouamane Laanait, Rama K. Vasudevan, and Stephen Jesse. USID and Pycroscopy – open source frameworks for storing and analyzing imaging and spectroscopy data. *Microscopy and Microanalysis*, 25(S2):220–221, 2019.
- [58] Chris Meyer, Niklas Dellby, Jordan A. Hachtel, Tracy Lovejoy, Andreas Mittelberger, and Ondrej Krivanek. Nion Swift: Open source image processing software for instrument control, data acquisition, organization, visualization, and analysis using python. *Microscopy and Microanalysis*, 25(S2):122–123, 2019.
- [59] Chu-Ping Yu, Thomas Friedrich, Daen Jannis, Sandra Van Aert, and Johan Verbeeck. Real-time integration center of mass (riCOM) reconstruction for 4D STEM. *Microscopy and Microanalysis*, 28(5):1526–1537, 2022.
- [60] Timothy J. Pennycook, Gerardo T. Martinez, Colum M. O’Leary, Hao Yang, and Peter D. Nellist. Efficient phase contrast imaging via electron ptychography, a tutorial. *Microscopy and Microanalysis*, 25(S2):2684–2685, 2019.
- [61] Mike Folk, Gerd Heber, Quincey Koziol, Elena Pourmal, and Dana Robinson. An overview of the HDF5 technology suite and its applications. In *Proceedings of the EDBT/ICDT 2011 Workshop on Array Databases*, pages 36–47, 2011.
- [62] J. D. Hunter. Matplotlib: A 2D graphics environment. *Computing in Science & Engineering*, 9(3):90–95, 2007.
- [63] Duncan Johnstone, Phillip Crout, Magnus Nord, Carter Francis, Joonatan Laulainen, Simon Høgås, Eirik Opheim, Ben Martineau, Tina Bergh, Eric Prestat, Niels Cautaerts, Stef Smeets, Håkon Wiik Ånes, Ross Andrew, Joseph Broussard, Sean Collins, Tom Furnival, Daen Jannis, Ida Hjorth, Mohsen Danaie, Andrew

Herzing, Endre Jacobsen, Tim Poon, Tiarnan Doherty, Shuoyuan Huang, Jedrzej Morzy, Affan Iqbal, Tomas Ostasevicius, Matt von Lany, and Rob Tovey. pyxem/pyxem: pyxem 0.14.2. Zenodo, 2022.

- [64] D. B. Williams and C. B. Carter. *Transmission electron microscopy: A textbook for materials science*. Springer, New York, NY, 2009.
- [65] A. P. Pogany and P. S. Turner. Reciprocity in electron diffraction and microscopy. *Acta Crystallographica Section A: Crystal Physics Diffraction Theoretical and General Crystallography*, 24(1):103–109, 1968.
- [66] Shoucong Ning, Wenhui Xu, Yinhang Ma, Leyi Loh, Timothy J. Pennycook, Wu Zhou, Fucui Zhang, Michel Bosman, Stephen J. Pennycook, Qian He, and N. Duane Loh. Accurate and robust calibration of the uniform affine transformation between scan-camera coordinates for atom-resolved in-focus 4D-STEM datasets. *Microscopy and Microanalysis*, 28(3):622–632, 2022.
- [67] A. J. Craven and T. W. Buggy. Design considerations and performance of an analytical STEM. *Ultramicroscopy*, 7(1):27–37, 1981.
- [68] S. D. Findlay, Yuji Kohno, L. A. Cardamone, Yuichi Ikuhara, and Naoya Shibata. Enhanced light element imaging in atomic resolution scanning transmission electron microscopy. *Ultramicroscopy*, 136:31–41, 2014.
- [69] Eric G. T. Bosch and Ivan Lazić. Analysis of HR-STEM theory for thin specimen. *Ultramicroscopy*, 156:59–72, 2015.
- [70] Dillan J. Chang, Colum M. O’Leary, Cong Su, Daniel A. Jacobs, Salman Kahn, Alex Zettl, Jim Ciston, Peter Ercius, and Jianwei Miao. Deep-learning electron diffractive imaging. *Physical Review Letters*, 130(1):016101, 2023.
- [71] Philipp M. Pelz, Ian Johnson, Colin Ophus, Peter Ercius, and Mary C. Scott. Real-time interactive 4D-STEM phase-contrast imaging from electron event representation data: Less computation with the right representation. *IEEE Signal Processing Magazine*, 39(1):25–31, 2021.

Sample	Gold Nanoparticle-modified DNA		Monolayer MoS ₂
Dataset Name	GP (infocus)	GP (underfocus)	MoS ₂
Accelerate Voltage (kV)	60	60	60
α (mrad)	22.5	22.5	22.5
Scanning Step Size (nm)	1.80	1.80	0.029
Defocus (μm)	-	2.11	-
Dwell Time (ms)	1.0	1.0	1.0
Diffraction Image Size	128×128	128×128	128×128
Scanning Positions	256×256	256×256	128×128
Preset Scanning Rotation ($^\circ$)	30	30	0

Table 1: Parameters of the experiment datasets.

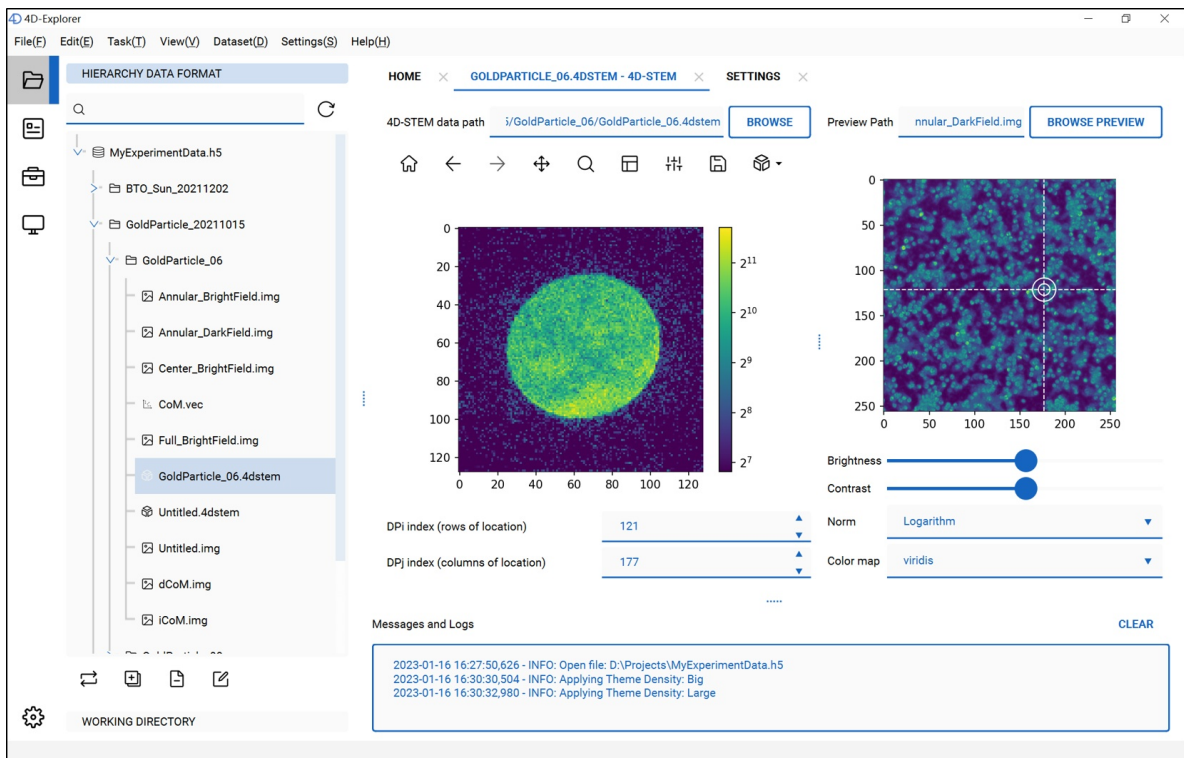


Figure 1: A screenshot of the main window of 4D-Explorer. A tree view at the left displays datasets stored in an HDF5 file. The main window is showing the 4D-STEM dataset of gold nanoparticle-modified DNA sample. In the middle is a diffraction pattern, while the right half is the reconstructed annular dark field (ADF) image.

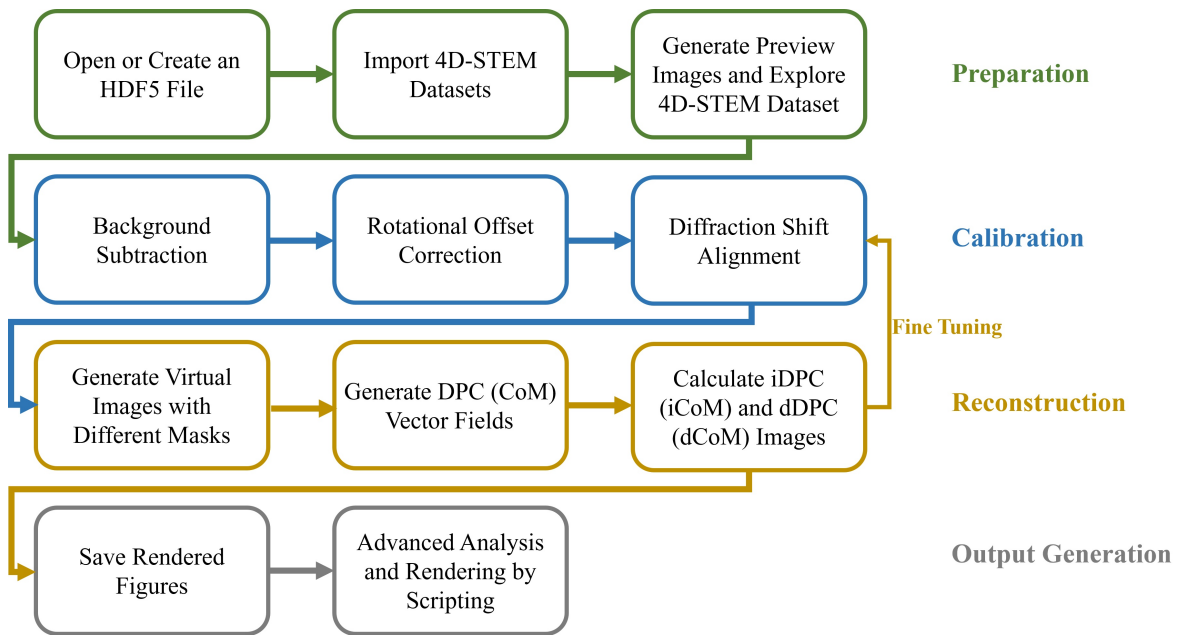


Figure 2: Workflow for 4D-STEM datasets analysis in 4D-Explorer. First in the preparation step, we load raw 4D-STEM dataset into the file manager. Then, we calibrate the dataset for physically meaningful and accurate images. Next, reconstruction algorithms are used to compute images. These images can also be used as basis for fine tuning. Finally results are rendered by appropriate viewers. They can then be displayed and saved for advanced analysis.

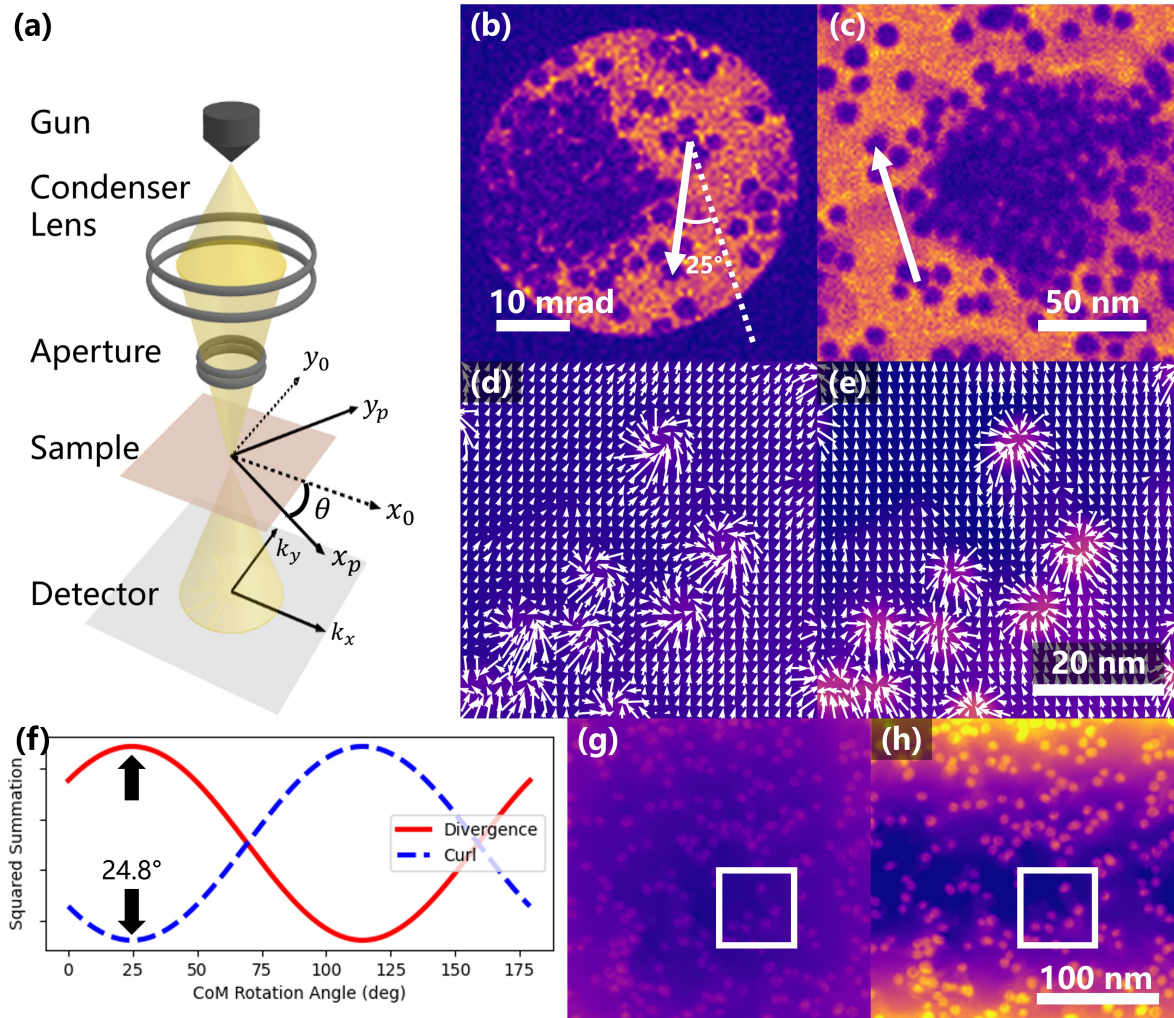


Figure 3: Rotational offset correction. (a) Schema of rotational offset during the 4D-STEM experiment. The probe is scanning along the x_0 and y_0 axes, which are not parallel to respective axes of the pixel arrays of the detector (k_x and k_y). (b,c) An underfocused 4D-STEM dataset of gold nanoparticles, including (b) diffraction pattern and (c) virtual Axial BF image. (d,e,g,h) Focused 4D-STEM dataset of gold nanoparticles before and after rotational offset correction, including (d) CoM before correction, (e) CoM after correction, (g) iCoM before correction and (h) iCoM after correction. (f) divergence and curl curve of the CoM field with respect to the rotation angle.

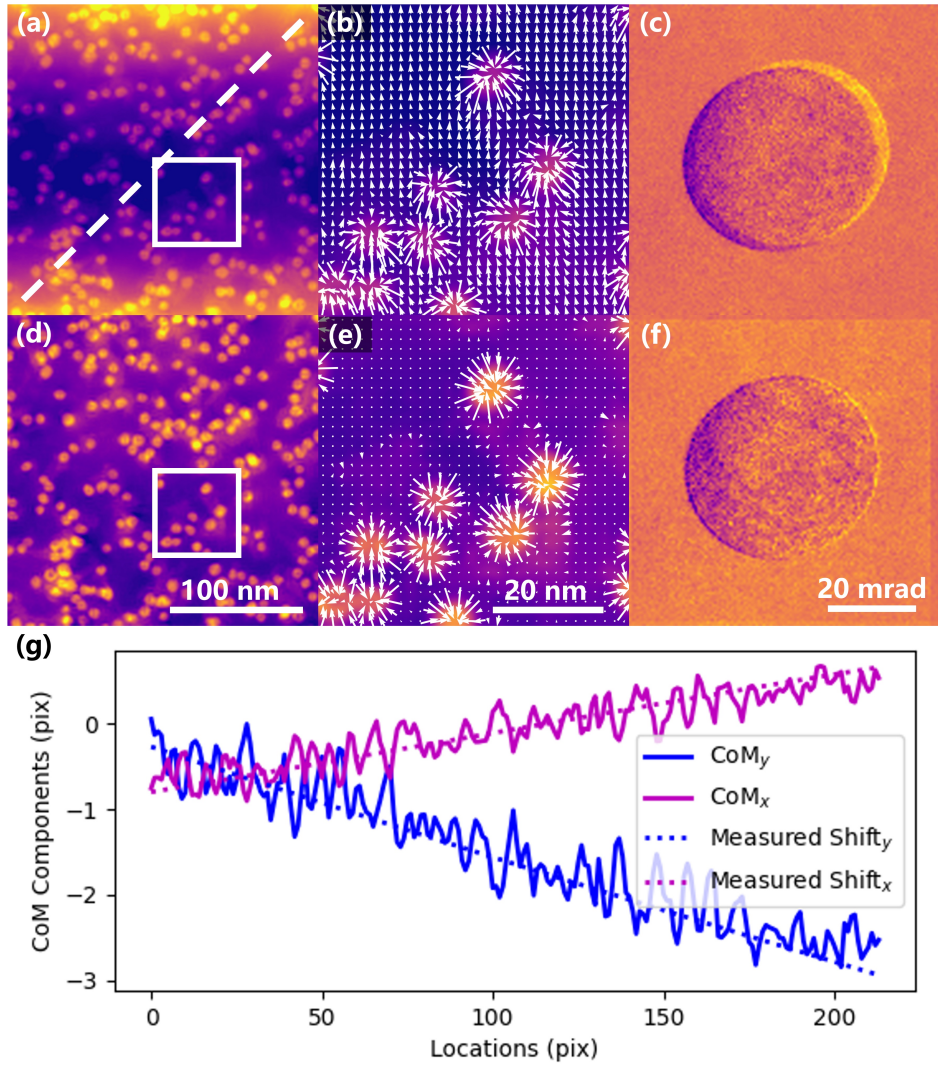


Figure 4: Diffraction alignment. (a-c) before alignment, (a) iCoM image. (b) the zoomed-in CoM distribution with iCoM as background of (a). (c) difference between diffraction patterns at the both ends of the dashed line in (a). (d-f) after alignment, corresponding images to (a-c). (g) line profile of CoM components and measured shift curve with respect to the dashed line in (a).

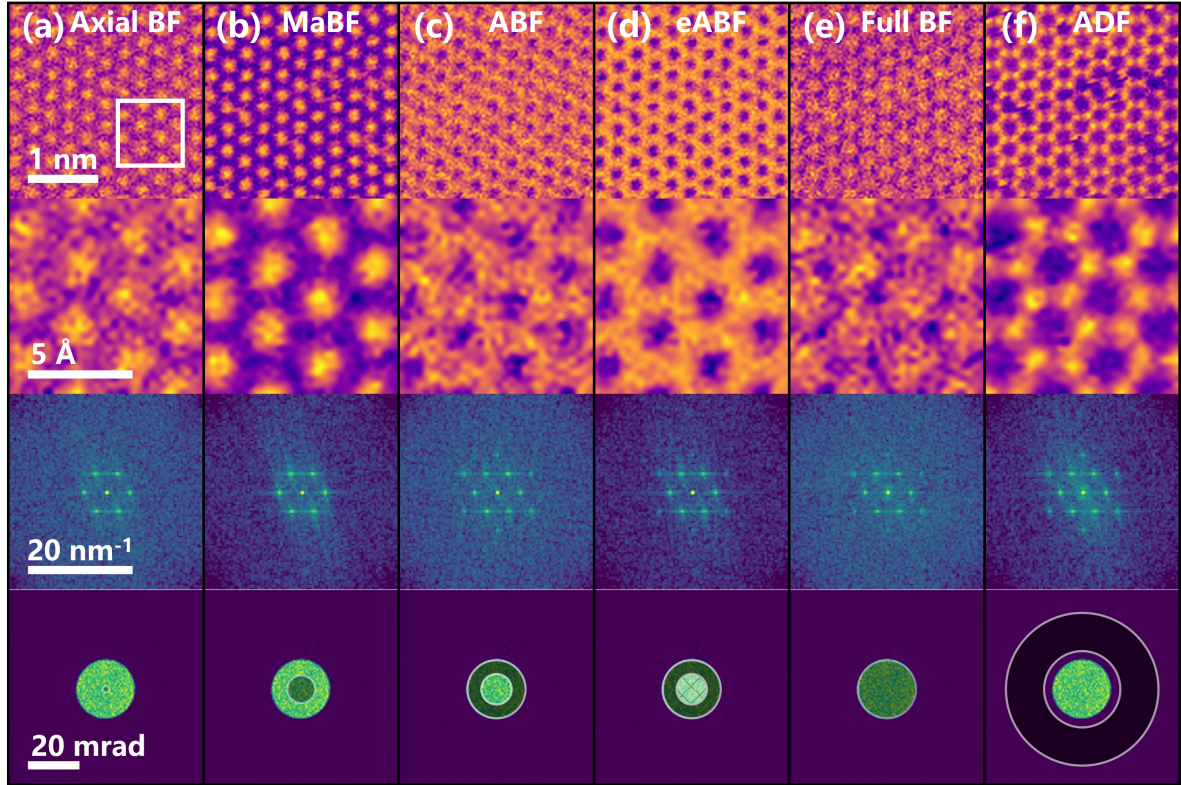


Figure 5: Virtual Imaging. Reconstructions using (a) axial bright field (Axial BF), (b) middle angle bright field (MaBF), (c) annular bright field (ABF), (d) enhanced annular bright field (eABF), (e) full bright field (Full BF) and (f) annular dark field (ADF). The four rows are reconstructed images, the zoomed-in images of the white square region in (a), power spectrums and diffraction patterns with virtual detectors (ROIs), respectively.

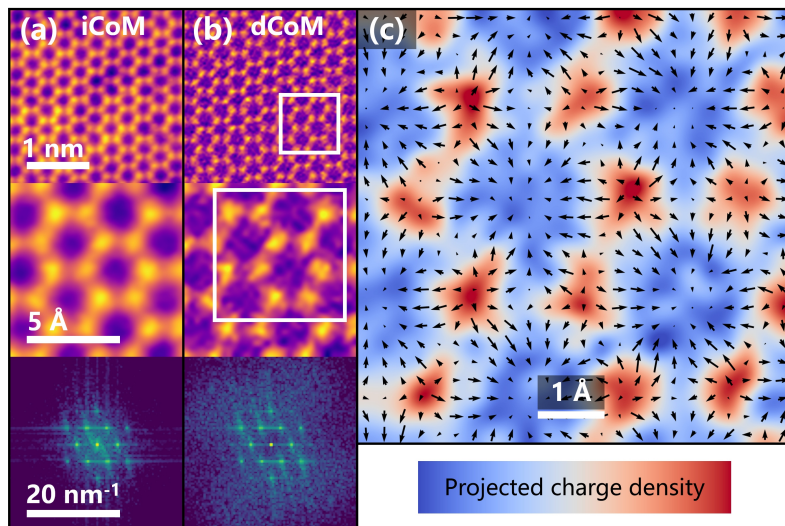


Figure 6: CoM reconstruction. (a) Differentiated CoM (dCoM). (b) Integrated CoM (iCoM). The three rows are reconstructed images, the zoomed-in images of the white square region in (a), and power spectrums. (c) CoM vector fields with projected charge density as the background image.

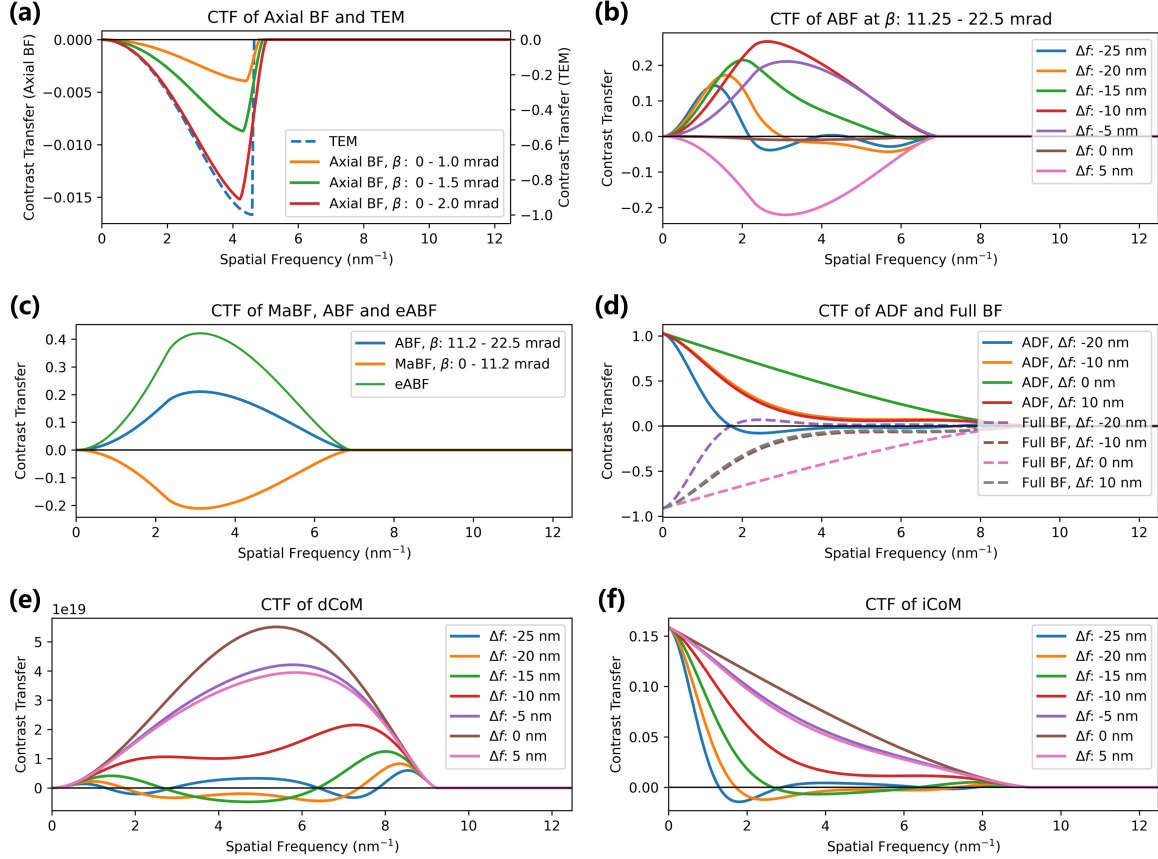


Figure 7: Contrast Transfer Functions of Virtual Imaging. The convergent semi-angle $\alpha = 22.5$ mrad, corresponding to spatial frequency 4.62 nm^{-1} . In all the calculations, we added a spherical aberration $C_S = 1 \mu\text{m}$. (a) Axial BF, LaBF, MaBF and TEM (in reciprocity) with defocus $\Delta f = -5 \text{ nm}$. (b) ABF using collection semi-angle β from 11.25 mrad to 22.5 mrad. (c) MaBF, ABF and eABF with defocus $\Delta f = -5 \text{ nm}$. (d) Full BF and ADF. The CTFs of ADF are calculated using collection semi-angle β from 27 mrad to 67.5 mrad. Note that the CTF of Full BF and ADF are calculated respect to the object $1 - \cos \phi$, which approximates to $\frac{1}{2}\phi^2$ when ϕ is small [69]. (e) dCoM with different defocus. (f) iCoM with different defocus.

Supplementary Information

4D-Explorer: a visual software for 4D-STEM data processing and image reconstruction

Hu Yiming et al.

1 Basic Formulation of 4D-STEM Imaging

Here we give a brief description of the 4D-STEM theory. A detailed introduction to 4D-STEM can be found in [1]. The wave function of the electron beam, after emitting from the source, is modified by the condenser lens and the aperture, noted as

$$\psi(\mathbf{u}) = C_A(\mathbf{u})E(\mathbf{u})e^{-i\chi(\mathbf{u})} \quad (\text{S1})$$

where $\mathbf{u} = (u_x, u_y)$ denotes the location of the back focal plane (BFP) of the condenser lens, $E(\mathbf{u})$ is the envelope function, and $\chi(\mathbf{u})$ is the aberration function. A is a subset of \mathbb{R}^2 and defined as

$$A = \left\{ \mathbf{u} \in \mathbb{R}^2 \mid |u| \leq \frac{\alpha}{\lambda} \right\} \quad (\text{S2})$$

where α is the convergent semi-angle, and λ is the wavelength of the beam. C_A is the characteristic function¹ of A . Hence,

$$C_A(\mathbf{u}) = \begin{cases} 1, & |\mathbf{u}| \leq \alpha/\lambda \\ 0, & |\mathbf{u}| > \alpha/\lambda \end{cases} \quad (\text{S3})$$

We can also denote $u_{\text{BF}} = \alpha/\lambda$, which is the radius of the bright field disk on the detector plane.

The wave front propagating to the image plane acts as the probe transmitting the sample. According to the scalar diffraction theory, it can be written as $\psi_{\text{in}}(\mathbf{r}) = \mathcal{F}[\psi(\mathbf{u})](\mathbf{r})$, where \mathcal{F} denotes the Fourier transform². The interaction between the electron beam and the thin specimen can be abstracted to input wave multiplying a transmission function $t(\mathbf{r})$ around the scanning point \mathbf{r}_p ,

$$\psi_{\text{out}}(\mathbf{r}; \mathbf{r}_p) = \psi_{\text{in}}(\mathbf{r})t(\mathbf{r}; \mathbf{r}_p) = \psi_{\text{in}}(\mathbf{r})e^{i\phi(\mathbf{r}+\mathbf{r}_p)} \quad (\text{S4})$$

where $\phi(\mathbf{r})$ is the modulating phase-change function of the sample, which is irrelative to the scanning point. For non-magnetic thin samples, the phase change is proportional to the projected potential

$$\phi(\mathbf{r}) = \sigma \int V(\mathbf{r}, z)dz = \frac{2\pi me\lambda}{h^2} \int V(\mathbf{r}, z)dz \quad (\text{S5})$$

where σ is called interaction parameter, e is charge, m is relativistic mass, and h is Planck's constant.

¹Characteristic functions are defined as $C_S(\mathbf{r}) = \begin{cases} 1, & \mathbf{r} \in S \\ 0, & \mathbf{r} \notin S \end{cases}$ for any subset $S \subset \mathbb{R}^2$.

²The Fourier transform is defined as $\mathcal{F}[f(\mathbf{r})](\mathbf{u}) = \int_{\mathbb{R}^2} f(\mathbf{r})e^{-2\pi i\mathbf{u}\cdot\mathbf{r}} d^2\mathbf{r}$, and the inverse Fourier transform is $\mathcal{F}^{-1}[g(\mathbf{u})](\mathbf{r}) = \int_{\mathbb{R}^2} g(\mathbf{u})e^{2\pi i\mathbf{u}\cdot\mathbf{r}} d^2\mathbf{u}$.

Then, following the scalar far-field diffraction theory again, the wave propagating to the detector plane is written as

$$\psi_D(\mathbf{u}; \mathbf{r}_p) = \mathcal{F}[\psi_{\text{out}}(\mathbf{r}; \mathbf{r}_p)](\mathbf{u}; \mathbf{r}_p) = \mathcal{F}[\psi_{\text{in}}(\mathbf{r})](\mathbf{u}) * \mathcal{F}[t(\mathbf{r}; \mathbf{r}_p)](\mathbf{u}; \mathbf{r}_p) \quad (\text{S6})$$

where $*$ is the convolution operator³.

The intensity that can be recorded by the detector is

$$I_D(\mathbf{u}; \mathbf{r}_p) = |\psi_D(\mathbf{u}; \mathbf{r}_p)|^2 \quad (\text{S7})$$

Sampling I_D produces a 4D-STEM dataset $I_D(n_x, n_y; m_x, m_y)$, where (n_x, n_y) is the coordinate of one diffraction image, and (m_x, m_y) indicates the specific diffraction image that corresponds to the scanning point \mathbf{r}_p .

2 Virtual Imaging

Virtual images are produced by integrating I_D over circular or annular regions on the diffraction plane for each scanning point \mathbf{r}_p . The analysis of the contrast of virtual images can be performed by the same process as conventional STEM, and has been introduced in [2]. Here for integrity we provide primary analysis and note the main properties. Detailed analysis of virtual image contrast can be found in [3].

We start with subsets $D = \{\mathbf{u} \in \mathbb{R}^2 | u_{\min} \leq |\mathbf{u}| \leq u_{\max}\}$ that describe virtual detectors, and $C_D(\mathbf{u})$ as their corresponding characteristic functions. For BF detectors, $u_{\min} = 0$ and $u_{\max} \leq u_{\text{BF}}$. For ABF detectors, $u_{\min} > 0$ and $u_{\max} \leq u_{\text{BF}}$. For ADF detectors, $u_{\max} > u_{\min} > u_{\text{BF}}$. Then, the reconstructed image can be written as

$$I_{\text{VI}}(\mathbf{r}_p) = \int_{\mathbf{u} \in S_D} I_D(\mathbf{u}; \mathbf{r}_p) d^2\mathbf{u} = \int_{\mathbb{R}^2} I_D(\mathbf{u}; \mathbf{r}_p) C_D(\mathbf{u}) d^2\mathbf{u} \quad (\text{S8})$$

The 4D-Explorer software uses the discrete version of the Equation (S8) to reconstruct virtual images.

Our analysis of virtual imaging follows [3]. Substituting I_D with Equation (S7), we have that

$$I_{\text{VI}}(\mathbf{r}_p) = \int_{\mathbb{R}^2} \int_{\mathbb{R}^2} \int_{\mathbb{R}^2} C_D(\mathbf{u}) e^{-2\pi i \mathbf{u} \cdot (\mathbf{r}' - \mathbf{r})} \psi_{\text{in}}^*(\mathbf{r}) \psi_{\text{in}}(\mathbf{r}') e^{i\phi(\mathbf{r}' + \mathbf{r}_p)} e^{-i\phi(\mathbf{r} + \mathbf{r}_p)} d^2\mathbf{r} d^2\mathbf{r}' d^2\mathbf{u} \quad (\text{S9})$$

Substituting with $K(\mathbf{r}; \mathbf{r}_p) = e^{i\phi(\mathbf{r} + \mathbf{r}_p)} - 1$, we have that

$$I_{\text{VI}}(\mathbf{r}_p) = \iiint_{\mathbb{R}^6} C_D |\psi_{\text{in}}|^2 e^{-2\pi i \mathbf{u} \cdot (\mathbf{r}' - \mathbf{r})} (1 + K(\mathbf{r}'; \mathbf{r}_p) + K^*(\mathbf{r}; \mathbf{r}_p) + K(\mathbf{r}'; \mathbf{r}_p) K^*(\mathbf{r}; \mathbf{r}_p)) d^2\mathbf{r} d^2\mathbf{r}' d^2\mathbf{u} \quad (\text{S10})$$

Since then, we can write the I_{VI} into four terms

$$I_{\text{VI}}(\mathbf{r}_p) = I_0(\mathbf{r}_p) + I_K(\mathbf{r}_p) + I_{K^*}(\mathbf{r}_p) + I_{KK^*}(\mathbf{r}_p) \quad (\text{S11})$$

Now we analyze the four terms respectively. The first term is that

$$I_0 = \int_{\mathbb{R}^2} C_D(\mathbf{u}) |\mathcal{F}[\psi_{\text{in}}]|^2 d^2\mathbf{u} \quad (\text{S12})$$

³The convolution operator is defined as $[f(\mathbf{r}') * g(\mathbf{r}')](\mathbf{r}) = \int_{\mathbb{R}^2} f(\mathbf{r}') g(\mathbf{r} - \mathbf{r}') d^2\mathbf{r}'$.

which is a constant and does not contribute to the contrast.

The next two terms are that

$$I_K(\mathbf{r}_p) = \int_{\mathbb{R}^2} \psi_{\text{in}}(\mathbf{r}) K(\mathbf{r}; \mathbf{r}_p) \mathcal{F} [C_D(\mathbf{u}) \mathcal{F}^{-1} [\psi_{\text{in}}^*(\mathbf{r}')] (\mathbf{u})] (\mathbf{r}) d^2\mathbf{r} \quad (\text{S13})$$

and

$$I_{K^*}(\mathbf{r}_p) = \int_{\mathbb{R}^2} \psi_{\text{in}}(\mathbf{r})^* K^*(\mathbf{r}; \mathbf{r}_p) \mathcal{F}^{-1} [C_D(\mathbf{u}) \mathcal{F} [\psi_{\text{in}}(\mathbf{r}')] (\mathbf{u})] (\mathbf{r}) d^2\mathbf{r} \quad (\text{S14})$$

For convenience, let

$$B(\mathbf{r}) = \psi_{\text{in}}(\mathbf{r}) \mathcal{F} [C_D(\mathbf{u}) \mathcal{F}^{-1} [\psi_{\text{in}}^*(\mathbf{r}')] (\mathbf{u})] (\mathbf{r}) \quad (\text{S15})$$

and we have that

$$\begin{aligned} I_K(\mathbf{r}_p) + I_{K^*}(\mathbf{r}_p) &= \int_{\mathbb{R}^2} K(\mathbf{r}; \mathbf{r}_p) B(\mathbf{r}) d^2\mathbf{r} + \int_{\mathbb{R}^2} K^*(\mathbf{r}; \mathbf{r}_p) B^*(\mathbf{r}) d^2\mathbf{r} \\ &= \frac{1}{2} \int_{\mathbb{R}^2} ((K + K^*) (B + B^*) + (K - K^*) (B - B^*)) d^2\mathbf{r} \end{aligned} \quad (\text{S16})$$

Note that $(B + B^*)/2$ and $(B - B^*)/(2i)$ are real part and imaginary part of B respectively, hence

$$I_K + I_{K^*} = -2 \int_{\mathbb{R}^2} (1 - \cos \phi(\mathbf{r} + \mathbf{r}_p)) \text{Re}(B(\mathbf{r})) d^2\mathbf{r} - 2 \int_{\mathbb{R}^2} \sin \phi(\mathbf{r} + \mathbf{r}_p) \text{Im}(B(\mathbf{r})) d^2\mathbf{r} \quad (\text{S17})$$

We can use the cross-correlation⁴ to define that

$$I_C(\mathbf{r}_p) = -2[\text{Re}(B(\mathbf{r})) \star (1 - \cos \phi(\mathbf{r}))](\mathbf{r}_p) \quad (\text{S18})$$

and

$$I_S(\mathbf{r}_p) = -2[\text{Im}(B(\mathbf{r})) \star \sin \phi(\mathbf{r})](\mathbf{r}_p) \quad (\text{S19})$$

which are linear responses of $1 - \cos \phi$ and $\sin \phi$ as the object respectively. Now using I_C and I_S , the virtual imaging can be rewritten as

$$I_{\text{VI}}(\mathbf{r}_p) = I_0 + I_C(\mathbf{r}_p) + I_S(\mathbf{r}_p) + I_{KK^*}(\mathbf{r}_p) \quad (\text{S20})$$

The last term I_{KK^*} is that

$$I_{KK^*}(\mathbf{r}_p) = \int_{\mathbb{R}^2} \int_{\mathbb{R}^2} \psi_{\text{in}}^*(\mathbf{r}) \psi_{\text{in}}(\mathbf{r}') K(\mathbf{r}'; \mathbf{r}_p) K^*(\mathbf{r}; \mathbf{r}_p) \mathcal{F} [C_D(\mathbf{u})] (\mathbf{r}' - \mathbf{r}) d^2\mathbf{r} d^2\mathbf{r}' \quad (\text{S21})$$

Substituting with $\mathbf{r}'' = \mathbf{r}' - \mathbf{r}$, the I_{KK^*} can be written in the form of auto-correlation

$$I_{KK^*}(\mathbf{r}_p) = \int_{\mathbb{R}^2} [\psi_{\text{in}}(\mathbf{r}) K(\mathbf{r}; \mathbf{r}_p) \star \psi_{\text{in}}(\mathbf{r}) K(\mathbf{r}; \mathbf{r}_p)] (\mathbf{r}''; \mathbf{r}_p) \mathcal{F} [C_D(\mathbf{u})] (\mathbf{r}'') d^2\mathbf{r}'' \quad (\text{S22})$$

Further analysis requires additional approximation. According to [3], the auto-correlation of $\psi_{\text{in}} K$ will reach its maximum at $\mathbf{r}'' = \mathbf{0}$, but rapidly decays to 0 outside a very small radius. Therefore, we use a new function to replace the auto-correlation,

⁴Cross-correlation is defined as that for any function $f(\mathbf{r})$ and $g(\mathbf{r})$, $[f(\mathbf{r}) \star g(\mathbf{r})](\mathbf{r}') = \int_{\mathbb{R}^2} f^*(\mathbf{r}) g(\mathbf{r}' + \mathbf{r}) d^2\mathbf{r}$

which remains the maximum value inside the small disk with radius ρ , while equals zero elsewhere. For amorphous carbon sample, $\rho = 0.090$ nm, while for periodic system, $\rho = 0.055$ nm. We use C_{S_ρ} to denote the characteristic function of the small disk, and then the auto-correlation can be written as

$$[\psi_{\text{in}}(\mathbf{r})K(\mathbf{r}; \mathbf{r}_p) \star \psi_{\text{in}}(\mathbf{r})K(\mathbf{r}; \mathbf{r}_p)](\mathbf{r}''; \mathbf{r}_p) \approx |\psi_{\text{in}}(\mathbf{r})|^2 |K(\mathbf{r}; \mathbf{r}_p)|^2 C_{S_\rho}(\mathbf{r}'') \quad (\text{S23})$$

Hence, the I_{KK^*} is that

$$I_{KK^*}(\mathbf{r}_p) \approx [|\psi_{\text{in}}(\mathbf{r})|^2 \star 2(1 - \cos \phi(\mathbf{r}))](\mathbf{r}_p) \int_{\mathbb{R}^2} C_{S_\rho}(\mathbf{r}'') \mathcal{F}[C_D(\mathbf{u})](\mathbf{r}'') d^2 \mathbf{r}'' \quad (\text{S24})$$

which is also a linear response of $1 - \cos \phi$. The integration

$$G_D = \int_{\mathbb{R}^2} C_{S_\rho}(\mathbf{r}'') \mathcal{F}[C_D(\mathbf{u})](\mathbf{r}'') d^2 \mathbf{r}'' = J_0\left(\frac{2\pi}{\lambda} \beta_{\text{min}} \rho\right) - J_0\left(\frac{2\pi}{\lambda} \beta_{\text{max}} \rho\right) \quad (\text{S25})$$

is a constant, in which J_0 is the Bessel function of the first kind and zero order.

Since I_{VI} can be regarded as linear responses of $\sin \phi$ and $1 - \cos \phi$ as objects, we can write its contrast transfer function for each object.

Detector Covering the Whole Plane When the virtual detector covers all of the detector plane, i.e. $C_D = 1$ everywhere, the $B(\mathbf{r}) = |\psi_{\text{in}}|^2$, and

$$I_S(\mathbf{r}_p) = 0, \quad I_C(\mathbf{r}_p) = -2 [|\psi_{\text{in}}|^2 \star (1 - \cos \phi(\mathbf{r}))](\mathbf{r}_p) \quad (\text{S26})$$

On the other hand, the last term of virtual imaging

$$I_{KK^*}(\mathbf{r}_p) = \int_{\mathbb{R}^2} \int_{\mathbb{R}^2} \psi_{\text{in}}^*(\mathbf{r}) \psi_{\text{in}}(\mathbf{r}') K(\mathbf{r}'; \mathbf{r}_p) K^*(\mathbf{r}; \mathbf{r}_p) \delta(\mathbf{r}' - \mathbf{r}) d^2 \mathbf{r} d^2 \mathbf{r}' \quad (\text{S27})$$

which is in fact

$$I_{KK^*} = 2 [|\psi_{\text{in}}|^2 \star (1 - \cos \phi(\mathbf{r}))](\mathbf{r}_p) \quad (\text{S28})$$

and hence vanishes along with I_C . Therefore, in this case there is no contrast at all

$$I_{\text{Full Plane}}(\mathbf{r}_p) = I_0 \quad (\text{S29})$$

which is in our expectation because we have collected all of the electrons from the beam.

(Annular) Bright Field When the virtual detector covers part of the bright field disk, i.e. $0 \leq \beta_{\text{min}} < \beta_{\text{max}} < \alpha$, BF and ABF images can be generated. Specifically, for $\beta_{\text{min}} = 0$ and $\beta_{\text{max}} = \alpha/2$, MaBF images are generated. Using weak phase object approximation (WPOA), we have that $\sin \phi \approx \phi$ and $1 - \cos \phi \approx 1$, so only I_S contributes to the contrast. The image of bright field and annular bright field can be written as

$$I_{\text{BF}}(\mathbf{r}_p) = I_0 - 2 [\text{Im}(\psi_{\text{in}}(\mathbf{r}) \mathcal{F}[C_D(\mathbf{u}) \mathcal{F}^{-1}[\psi_{\text{in}}^*(\mathbf{r}')](\mathbf{u})](\mathbf{r})) \star \sin \phi(\mathbf{r})](\mathbf{r}_p) \quad (\text{S30})$$

and the contrast transfer function is

$$T_{\text{BF}}(\mathbf{u}) = -2 \mathcal{F}^*[\text{Im}(\psi_{\text{in}} \mathcal{F}[C_D \mathcal{F}^{-1}[\psi_{\text{in}}^*])](\mathbf{u})] \quad (\text{S31})$$

Annular Dark Field When the virtual detector does not coincide with the bright field disk, i.e. $0 < \alpha \leq \beta_{\min} < \beta_{\max}$, ADF images can be generated. Since $A(\mathbf{k})C_D(\mathbf{u}) = 0$, we have that

$$C_D(\mathbf{u})\mathcal{F}^{-1}[\psi_{\text{in}}^*] = C_D(\mathbf{u})A(\mathbf{u})E(\mathbf{u})e^{i\chi(\mathbf{u})} = 0 \quad (\text{S32})$$

Hence, only I_{KK^*} contributes to the contrast

$$I_{\text{ADF}}(\mathbf{r}_p) = 2G_D [|\psi_{\text{in}}(\mathbf{r})|^2 \star (1 - \cos \phi(\mathbf{r}))] (\mathbf{r}_p) \quad (\text{S33})$$

where G_D is calculated from Equation (S25). Here, if we use WPOA, we will not generate any contrast from ADF, which is the reason why it is hard for ADF to image light element samples. Thus we need to retain terms up to second order, $1 - \cos \phi \approx \phi^2/2$ when ϕ is small. Using $1 - \cos \phi$ as the sample, the contrast transfer function of ADF is

$$T_{\text{ADF}}(\mathbf{u}) = 2G_D\mathcal{F}^* [|\psi_{\text{in}}|^2] (\mathbf{u}) \quad (\text{S34})$$

Full Bright Field When the virtual detector covers the entire bright field diffraction disk, i.e. $\beta_{\min} = 0$ and $\beta_{\max} = \alpha$, the image is written as

$$I_{\text{Full BF}}(\mathbf{r}_p) = I_0 + [(-2\text{Re}(\psi_{\text{in}}\mathcal{F}[C_D\mathcal{F}^{-1}[\psi_{\text{in}}^*]]) + 2G_D|\psi_{\text{in}}|^2) \star (1 - \cos \phi)] \quad (\text{S35})$$

The contrast of Full BF is opposite to the ADF's contrast, because it can be regarded as the difference between the image obtained by a virtual detector covering only the plane outside the bright field diffraction disk, and $I_{\text{Full Plane}}$ which is a constant. Therefore, using $1 - \cos \phi$ as the sample, its contrast transfer function is that

$$T_{\text{Full BF}}(\mathbf{r}_p) = 2\mathcal{F}^* [-\text{Re}(\psi_{\text{in}}\mathcal{F}[C_D\mathcal{F}^{-1}[\psi_{\text{in}}^*]]) + G_D|\psi_{\text{in}}|^2] \quad (\text{S36})$$

Enhanced Annular Bright Field According to [4], the enhanced annular bright field (eABF) is defined as the difference between the MaBF and ABF. Therefore, using WPOA, its image is that

$$I_{\text{eABF}}(\mathbf{r}_p) = I_0 - 2 [\text{Im}(\psi_{\text{in}}\mathcal{F}[(C_{D_{\text{ABF}}} - C_{D_{\text{MaBF}}})\mathcal{F}^{-1}[\psi_{\text{in}}^*]]) \star \sin \phi] (\mathbf{r}_p) \quad (\text{S37})$$

and its contrast transfer function is that

$$T_{\text{eABF}}(\mathbf{u}) = -2\mathcal{F}^* [\text{Im}(\psi_{\text{in}}\mathcal{F}[(C_{D_{\text{ABF}}} - C_{D_{\text{MaBF}}})\mathcal{F}^{-1}[\psi_{\text{in}}^*]])] (\mathbf{u}) \quad (\text{S38})$$

3 Axial Bright Field

The depth of field of BF, ABF and ADF is usually narrow compared to CTEM images. However, Axial BF virtual detector produces images that have similar properties to CTEM, including a wide depth of field. This is from the principal of reciprocity [3, 5].

By substituting Dirac's delta function⁵ $\delta(\mathbf{u})$ to the virtual detector in Equation (S8), we have that

$$I_{\text{Axial BF}}(\mathbf{r}_p) = \int_{\mathbb{R}^2} I_D(\mathbf{u}; \mathbf{r}_p)\delta(\mathbf{u})d^2\mathbf{u} = \left| \int_{\mathbb{R}^2} \psi_{\text{in}}(\mathbf{r})e^{i\phi(\mathbf{r}+\mathbf{r}_p)}d^2\mathbf{r} \right|^2 \quad (\text{S39})$$

⁵Dirac delta function $\delta(\mathbf{r})$ is defined as that for any function $f(\mathbf{r})$, $\int_{\mathbb{R}^2} f(\mathbf{r})\delta(\mathbf{r})d^2\mathbf{r} = f(\mathbf{0})$.

which is exactly the same as the conventional flipped TEM image by substituting \mathbf{r}_p with $-\mathbf{r}_p$

$$I_{\text{Axial BF}}(-\mathbf{r}_p) = \left| [e^{i\phi(\mathbf{r})} * \mathcal{F}[\psi(\mathbf{u})]](\mathbf{r}_p) \right|^2 \quad (\text{S40})$$

which has the same form as the image of HRTEM [6]. By substituting $C_D(\mathbf{u})$ with $\delta(\mathbf{u})$ in Equation (S31) [3], we have that

$$T_{\text{Axial BF}}(\mathbf{u}) = -2\mathcal{F}^* [\text{Im}(\psi_{\text{in}} \mathcal{F}[\delta(\mathbf{u}) \mathcal{F}^{-1}[\psi_{\text{in}}^*]])](\mathbf{u}) = -2\mathcal{F}^* [\text{Im}(\psi_{\text{in}})] \quad (\text{S41})$$

and hence

$$T_{\text{Axial BF}}(\mathbf{u}) = 2C_A(-\mathbf{u})E(-\mathbf{u})\sin(\chi(-\mathbf{u})) \quad (\text{S42})$$

In 4D-Explorer, we usually use a narrow bright field detector (for example, a single centered pixel of the diffraction image) to generate the axial BF images, and to approximate CTEM images.

4 Center of Mass Imaging

There are two methods to produce differential phase contrast (DPC) [7]. One is setting segmented virtual detectors and calculating differences of signals in the opposite orientations. This method is widely used, especially when pixelated electron detectors are not available. The other is to calculate the center of mass (CoM) of the bright field disk. It is also known as the first momentum imaging. In 4D-Explorer the default method to produce DPC vector fields is CoM, i.e. calculating center of mass of the bright field disk

$$\mathbf{I}_{\text{CoM}}(\mathbf{r}_p) = \int_{\mathbb{R}^2} \mathbf{u} I_{\text{D}}(\mathbf{k}; \mathbf{r}_p) d^2\mathbf{u} \quad (\text{S43})$$

which is a field distribution on the sample plane. Thus we can compute its divergence

$$I_{\text{dCoM}}(\mathbf{r}_p) = \nabla_p \cdot \mathbf{I}_{\text{CoM}}(\mathbf{r}_p) = \frac{\partial I_{\text{CoM}x}(\mathbf{r}_p)}{\partial x_p} + \frac{\partial I_{\text{CoM}y}(\mathbf{r}_p)}{\partial y_p} \quad (\text{S44})$$

as differentiated CoM (dCoM), and its potential $I_{i\text{CoM}}(\mathbf{r}_p)$ satisfying that

$$\mathbf{I}_{\text{CoM}}(\mathbf{r}_p) = \nabla_p I_{i\text{CoM}}(\mathbf{r}_p) = \left(\frac{\partial I_{i\text{CoM}}(\mathbf{r}_p)}{\partial x_p}, \frac{\partial I_{i\text{CoM}}(\mathbf{r}_p)}{\partial y_p} \right) \quad (\text{S45})$$

as integrated CoM (iCoM), if the vector field is conserved. By Stokes theorem, the conservative field requires that the curl of the field (cCoM)

$$I_{\text{cCoM}}(\mathbf{r}_p) = \nabla_p \times \mathbf{I}_{\text{CoM}}(\mathbf{r}_p) = \frac{\partial I_{\text{CoM}y}(\mathbf{r}_p)}{\partial x_p} - \frac{\partial I_{\text{CoM}x}(\mathbf{r}_p)}{\partial y_p} \quad (\text{S46})$$

equals zero everywhere.

Now we analyze the imaging of CoM. Following [7], we have that

$$I_{\text{CoM}x}(\mathbf{r}_p) = \int u_x \mathcal{F}[\psi_{\text{out}}(\mathbf{r}); \mathbf{r}_p](\mathbf{u}) \mathcal{F}^*[\psi_{\text{out}}(\mathbf{r}'; \mathbf{r}_p)](\mathbf{u}) d^2\mathbf{u} \quad (\text{S47})$$

Then, using the derivative formula of Fourier transform, we have that

$$u_x \mathcal{F}[f(\mathbf{r})] = \frac{1}{2\pi i} \mathcal{F} \left[\frac{\partial f(\mathbf{r})}{\partial x} \right] \quad (\text{S48})$$

and hence

$$I_{\text{CoM}x}(\mathbf{r}_p) = \frac{1}{2\pi i} \int_{\mathbb{R}^2} \mathcal{F} \left[\frac{\partial \psi_{\text{out}}(\mathbf{r}; \mathbf{r}_p)}{\partial x} \right] (\mathbf{u}) \mathcal{F} [\psi_{\text{out}}^*(-\mathbf{r}'; \mathbf{r}_p)] (\mathbf{u}) d^2\mathbf{u} \quad (\text{S49})$$

Considering the fact that for any function $f(\mathbf{r})$, its integration over the full plane

$$\int_{\mathbb{R}^2} f(\mathbf{r}) d^2\mathbf{r} = \mathcal{F} [f(\mathbf{r})] (\mathbf{u} = 0) \quad (\text{S50})$$

and using the convolution theorem,

$$I_{\text{CoM}x}(\mathbf{r}_p) = \frac{1}{2\pi i} \int_{\mathbb{R}^2} \frac{\partial \psi_{\text{out}}(\mathbf{r}; \mathbf{r}_p)}{\partial x} \psi_{\text{out}}^*(\mathbf{r}; \mathbf{r}_p) d^2\mathbf{r} \quad (\text{S51})$$

Now substituting ψ_{out} and $\frac{\partial \psi_{\text{out}}}{\partial x}$ with ψ_{in} and the transmission function of the sample, we have that

$$I_{\text{CoM}x}(\mathbf{r}_p) = \frac{1}{2\pi i} \int_{\mathbb{R}^2} \left(\frac{\partial \psi_{\text{in}}(\mathbf{r})}{\partial x} \psi_{\text{in}}^*(\mathbf{r}) + i\psi_{\text{in}}(\mathbf{r}) \psi_{\text{in}}^*(\mathbf{r}) \frac{\partial \phi(\mathbf{r} + \mathbf{r}_p)}{\partial x} \right) d^2\mathbf{r} \quad (\text{S52})$$

which can be written in the form of cross-correlation

$$I_{\text{CoM}x}(\mathbf{r}_p) = \frac{1}{2\pi i} \int_{\mathbb{R}^2} \frac{\partial \psi_{\text{in}}(\mathbf{r})}{\partial x} \psi_{\text{in}}^*(\mathbf{r}) d^2\mathbf{r} + \frac{1}{2\pi} \left[|\psi_{\text{in}}(\mathbf{r})|^2 \star \frac{\partial \phi(\mathbf{r})}{\partial x} \right] (\mathbf{r}_p) \quad (\text{S53})$$

The first term is actually a constant and does not contribute to the contrast. Therefore, the relationship between CoM fields and the object is that

$$\mathbf{I}_{\text{CoM}}(\mathbf{r}_p) = \frac{1}{2\pi} [|\psi_{\text{in}}(\mathbf{r})|^2 \star \nabla \phi(\mathbf{r})] (\mathbf{r}_p) \quad (\text{S54})$$

which is a linear response to the gradient of the projected potential of the sample, i.e. the local projected electric field. The dCoM images can be written as

$$I_{\text{dCoM}}(\mathbf{r}_p) = \frac{1}{2\pi} [|\psi_{\text{in}}(\mathbf{r})|^2 \star \nabla^2 \phi(\mathbf{r})] (\mathbf{r}_p) \quad (\text{S55})$$

which is a linear response to the laplacian of the projected potential of the sample, i.e. the local projected charge density. Also, the iCoM image can be written as

$$I_{\text{iCoM}}(\mathbf{r}_p) = \frac{1}{2\pi} [|\psi_{\text{in}}(\mathbf{r})|^2 \star \phi(\mathbf{r})] (\mathbf{r}_p) \quad (\text{S56})$$

which is a linear response to the projected potential of the sample, i.e. the phase contrast. This is the reason why DPC images are sensitive to both light and heavy atoms simultaneously with good interpretability.

Next, we analyze the contrast transfer functions of CoM image modes. Using the cross-correlation theorem, we have that

$$T_{\text{iCoM}}(\mathbf{u}) = \frac{1}{2\pi} \mathcal{F}^* [|\psi_{\text{in}}(\mathbf{r})|^2] (\mathbf{u}) \quad (\text{S57})$$

Based on the CTF of iCoM images and the differential and integral properties of Fourier transform, the CTF of CoM vector fields can be directly written as

$$\mathbf{T}_{\text{CoM}}(\mathbf{u}) = i\mathbf{u} \mathcal{F}^* [|\psi_{\text{in}}(\mathbf{r})|^2] (\mathbf{u}) \quad (\text{S58})$$

Here, the x and y components of $\mathbf{T}_{\text{CoM}}(\mathbf{u})$ are the contrast transfer functions of the CoM vector field in the x and y directions, respectively. Similarly, the CTF of dCoM images (respect to the object ϕ) can also be obtained

$$T_{\text{dCoM}}(\mathbf{u}) = -2\pi |u|^2 \mathcal{F}^* [|\psi_{\text{in}}(\mathbf{r})|^2] (\mathbf{u}) \quad (\text{S59})$$

At last, we prove that the curl of CoM field is always zero. The first term in the definition of cCoM Equation (S46) is written as

$$\frac{\partial I_{\text{CoMy}}}{\partial x_p} = \frac{1}{2\pi} \int_{\mathbb{R}^2} \psi_{\text{in}}(\mathbf{r}) \psi_{\text{in}}^*(\mathbf{r}) \frac{\partial}{\partial x_p} \frac{\partial}{\partial y} \phi(x + x_p, y + y_p) d^2\mathbf{r} \quad (\text{S60})$$

by substituting the contrast of CoM vector Equation (S54). Assume that $\phi = \phi(u, v)$, where u and v denotes the first argument and the second argument of function ϕ respectively. Then, we have that

$$\frac{\partial}{\partial x_p} \frac{\partial}{\partial y} \phi(x + x_p, y + y_p) = \frac{\partial}{\partial x_p} \frac{\partial \phi(x + x_p, v)}{\partial v} \bigg|_{v=y+y_p} \frac{d(y + y_p)}{dy} = \frac{\partial^2 \phi(u, v)}{\partial u \partial v} \bigg|_{u=x+x_p, v=y+y_p} \quad (\text{S61})$$

And due to the same reason of Equation (S61), for the second term of Equation (S46) we have that

$$\frac{\partial}{\partial y_p} \frac{\partial}{\partial x} \phi(x + x_p, y + y_p) = \frac{\partial^2 \phi(u, v)}{\partial v \partial u} \bigg|_{u=x+x_p, v=y+y_p} = \frac{\partial^2 \phi(u, v)}{\partial u \partial v} \bigg|_{u=x+x_p, v=y+y_p} \quad (\text{S62})$$

Therefore, the two terms vanish for any $\mathbf{r}_p \in \mathbb{R}^2$, and $I_{\text{cCoM}}(\mathbf{r}_p) = 0$.

5 Rotational Offset Correction using CoM

Rotational offsets between the scanning coordinate and the detector coordinate will affect the reconstructed images if they are not carefully corrected. Here, we provide the theory of correcting the rotational offset using properties of CoM vector fields. This method has the same physical origin as the J-Matrix method described in [8].

Let $(\mathbf{e}_{px}, \mathbf{e}_{py})$ be the orthonormal basis of the scanning plane, and $(\mathbf{e}_{0x}, \mathbf{e}_{0y})$ be the orthonormal basis of the detector plane, as shown in Supplementary Figure S2a. Then, a scanning position \mathbf{r}_p can be written as $\mathbf{r}_p = x_p \mathbf{e}_x + y_p \mathbf{e}_y$, where (x_p, y_p) is the coordinate of \mathbf{r}_p . Suppose there exists rotational offset with angle θ between the two planes such that

$$\begin{cases} \mathbf{e}_{0x} = \mathbf{e}_{px} \cos \theta + \mathbf{e}_{py} \sin \theta \\ \mathbf{e}_{0y} = -\mathbf{e}_{px} \sin \theta + \mathbf{e}_{py} \cos \theta \end{cases} \quad (\text{S63})$$

At each scanning point \mathbf{r}_p we receive a diffraction image, and we will calculate the center of mass of the images to reconstruct DPC images. If the rotational offset was not a major concern, we would use the following naïve formula to calculate CoM vectors which is incorrect:

$$\mathbf{I}_{\text{nCoM}}(\mathbf{r}_p) = I_{\text{CoMx}}(\mathbf{r}_p) \mathbf{e}_{px} + I_{\text{CoMy}}(\mathbf{r}_p) \mathbf{e}_{py} \quad (\text{S64})$$

That is because in computers the two directions of the scanning matrix and the detector matrix look the same. The subscript “nCoM” means the CoM vectors calculated by

the naïve method. However, as the camera rotated θ angle, the correct CoM vector at \mathbf{r}_p is

$$\mathbf{I}_{\text{CoM}}(\mathbf{r}_p) = I_{\text{CoM}x}(\mathbf{r}_p)\mathbf{e}_{0x} + I_{\text{CoM}y}(\mathbf{r}_p)\mathbf{e}_{0y} \quad (\text{S65})$$

If we are not aware of θ , no correct DPC reconstruction images can be generated, let alone other image modes such as ptychography or orientation mapping.

Fortunately, DPC itself provides us with a method to correct the rotational offset. This method is based on the fact that CoM vector fields is linear to the projected electrostatic field of the sample, which should be conservative and irrotative, as stated in Equation (S54). In this section we will prove that the rotational angle θ can be acquired by minimizing the sum of the squared curl of CoM vector field.

What we get through the detectors and CoM algorithms is the two components $I_{\text{CoM}x}(\mathbf{r}_p)$ and $I_{\text{CoM}y}(\mathbf{r}_p)$ that should be a linear combination of detector's basis \mathbf{e}_{0x} and \mathbf{e}_{0y} as stated in Equation (S65). Therefore, the correct dCoM is

$$\begin{aligned} I_{\text{dCoM}}(\mathbf{r}_p) &= \nabla_p \cdot (I_{\text{CoM}x}(\mathbf{r}_p)\mathbf{e}_{0x} + I_{\text{CoM}y}(\mathbf{r}_p)\mathbf{e}_{0y}) \\ &= \nabla_p \cdot (I_{\text{CoM}x}(\mathbf{e}_{px} \cos \theta + \mathbf{e}_{py} \sin \theta) + I_{\text{CoM}y}(-\mathbf{e}_{px} \sin \theta + \mathbf{e}_{py} \cos \theta)) \\ &= \left(\cos \theta \frac{\partial}{\partial x_p} + \sin \theta \frac{\partial}{\partial y_p} \right) I_{\text{CoM}x}(\mathbf{r}_p) + \left(-\sin \theta \frac{\partial}{\partial x_p} + \cos \theta \frac{\partial}{\partial y_p} \right) I_{\text{CoM}y}(\mathbf{r}_p) \\ &= \left(\frac{\partial x_p}{\partial x_0} \frac{\partial}{\partial x_p} + \frac{\partial y_p}{\partial x_0} \frac{\partial}{\partial y_p} \right) I_{\text{CoM}x}(\mathbf{r}_p) + \left(\frac{\partial x_p}{\partial y_0} \frac{\partial}{\partial x_p} + \frac{\partial y_p}{\partial y_0} \frac{\partial}{\partial y_p} \right) I_{\text{CoM}y}(\mathbf{r}_p) \\ &= \frac{\partial}{\partial x_0} I_{\text{CoM}x}(\mathbf{r}_p) + \frac{\partial}{\partial y_0} I_{\text{CoM}y}(\mathbf{r}_p) \end{aligned} \quad (\text{S66})$$

This is expected because the divergence operator is not related to a specific basis, and that $I_{\text{CoM}x}$ and $I_{\text{CoM}y}$ are components of the detector basis. Due to the same reason, the correct curl of CoM is

$$I_{\text{cCoM}}(\mathbf{r}_p) = \frac{\partial}{\partial x_0} I_{\text{CoM}y}(\mathbf{r}_p) - \frac{\partial}{\partial y_0} I_{\text{CoM}x}(\mathbf{r}_p) = 0 \quad (\text{S67})$$

which has been shown in Section 4.

Now we consider the wrong dCoM calculated using the naïve method Equation (S64). We have that

$$\begin{aligned} I_{\text{ndCoM}}(\mathbf{r}_p) &= \nabla_p \cdot (I_{\text{CoM}x}(\mathbf{r}_p)\mathbf{e}_{px} + I_{\text{CoM}y}(\mathbf{r}_p)\mathbf{e}_{py}) \\ &= \frac{\partial}{\partial x_p} I_{\text{CoM}x}(\mathbf{r}_p) + \frac{\partial}{\partial y_p} I_{\text{CoM}y}(\mathbf{r}_p) \\ &= \frac{\partial x_0}{\partial x_p} \frac{\partial I_{\text{CoM}x}}{\partial x_0} + \frac{\partial y_0}{\partial x_p} \frac{\partial I_{\text{CoM}x}}{\partial y_0} + \frac{\partial x_0}{\partial y_p} \frac{\partial I_{\text{CoM}y}}{\partial x_0} + \frac{\partial y_0}{\partial y_p} \frac{\partial I_{\text{CoM}y}}{\partial y_0} \\ &= \cos \theta \left(\frac{\partial I_{\text{CoM}x}}{\partial x_0} + \frac{\partial I_{\text{CoM}y}}{\partial y_0} \right) + \sin \theta \left(\frac{\partial I_{\text{CoM}y}}{\partial x_0} - \frac{\partial I_{\text{CoM}x}}{\partial y_0} \right) \\ &= I_{\text{dCoM}}(\mathbf{r}_p) \cos \theta + I_{\text{cCoM}}(\mathbf{r}_p) \sin \theta \\ &= I_{\text{dCoM}}(\mathbf{r}_p) \cos \theta \end{aligned} \quad (\text{S68})$$

The result of the wrong dCoM shows that when $\theta = 0$, i.e. there is no rotational offset, the contrast of dCoM image reaches maximum. This property is key to our rotational offset correction algorithms.

Meanwhile, we can also consider the wrong cCoM, which by similar process can be written as

$$\begin{aligned}
I_{\text{ncCoM}}(\mathbf{r}_p) &= \nabla_p \times (I_{\text{CoM}x} \mathbf{e}_{px} + I_{\text{CoM}y}(\mathbf{r}_p) \mathbf{e}_{py}) \\
&= \frac{\partial}{\partial x_p} I_{\text{CoM}y}(\mathbf{r}_p) - \frac{\partial}{\partial y_p} I_{\text{CoM}x}(\mathbf{r}_p) \\
&= \frac{\partial x_0}{\partial x_p} \frac{\partial I_{\text{CoM}y}}{\partial x_0} + \frac{\partial y_0}{\partial x_p} \frac{\partial I_{\text{CoM}y}}{\partial y_0} - \frac{\partial x_0}{\partial y_p} \frac{\partial I_{\text{CoM}x}}{\partial x_0} - \frac{\partial y_0}{\partial y_p} \frac{\partial I_{\text{CoM}x}}{\partial y_0} \\
&= \cos \theta \left(\frac{\partial I_{\text{CoM}y}}{\partial x_0} - \frac{\partial I_{\text{CoM}x}}{\partial y_0} \right) - \sin \theta \left(\frac{\partial I_{\text{CoM}y}}{\partial y_0} + \frac{\partial I_{\text{CoM}x}}{\partial x_0} \right) \\
&= I_{\text{cCoM}}(\mathbf{r}_p) \cos \theta - I_{\text{dCoM}}(\mathbf{r}_p) \sin \theta \\
&= -I_{\text{dCoM}}(\mathbf{r}_p) \sin \theta
\end{aligned} \tag{S69}$$

The result of the wrong cCoM shows that when $\theta = 0$, i.e. there is no rotational offset, cCoM does not have any contrast, which has been illustrated in Section 4. However, if there is rotational offset, the contrast of the cCoM images is proportional to dCoM, and reaches maximum when $\theta = \pi/2$. In this case, the reconstructed CoM vector fields becomes a non-divergent field with vortices around atoms.

The results from Equation (S68) and Equation (S69) provide us with a method to correct the rotational offset, where the angle θ that minimize the square sum of curl of CoM calculated from the naïve approach:

$$\theta = \arg \min_{\theta} \int_{\mathbb{R}^2} |I_{\text{ncCoM}}(\mathbf{r}_p; \theta)|^2 d^2 \mathbf{r}_p \tag{S70}$$

In practice, we try to rotate every CoM vector by an angle, and calculate its corresponding value of the target function. The rotation angle is the one minimizing the target function. Then, we can rotate every diffraction images with that angle and perform reconstruction processes as usual. Note that there exist two solutions θ generated by Equation (S70) differing π from each other. Only one θ of them is physically valid, while the other θ' corresponds to the case where atoms have negative charge density. A simple way to distinguish between the two solutions is to compare reconstructed iCoM image with ADF images. Since ADF images are not sensitive to rotational offset and have the contrast with the same sign as the projected potential, the θ that leads to the same contrast is the correct one.

References

- [1] Colin Ophus. Four-dimensional scanning transmission electron microscopy (4D-STEM): From scanning nanodiffraction to ptychography and beyond. *Microscopy and Microanalysis*, 25(3):563–582, 2019.
- [2] Stephen J. Pennycook and Peter D. Nellist. *Scanning transmission electron microscopy: Imaging and analysis*. Springer, New York, NY, 2011.
- [3] Eric G. T. Bosch and Ivan Lazić. Analysis of HR-STEM theory for thin specimen. *Ultramicroscopy*, 156:59–72, 2015.

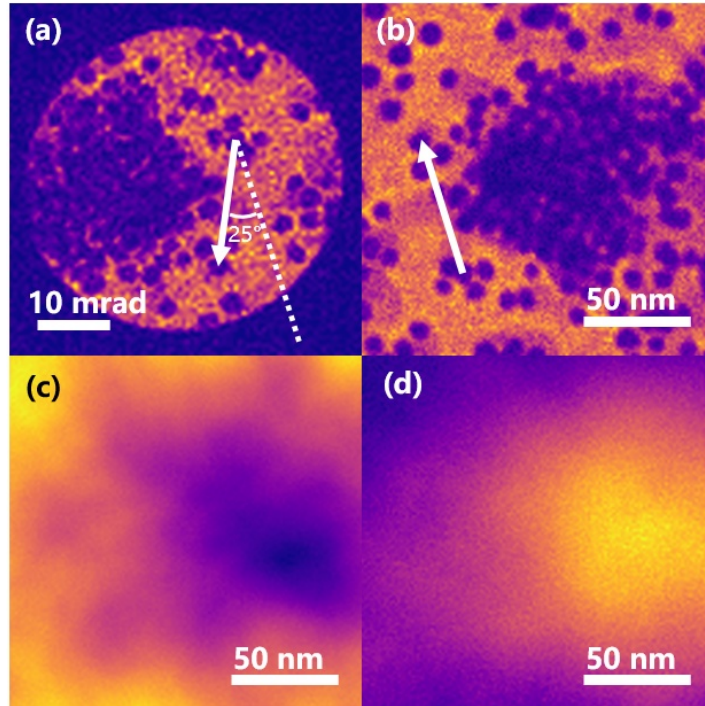


Figure S1: The defocused 4D-STEM dataset of gold nanoparticles: diffraction pattern and virtual images. (a) A diffraction pattern of the 4D-STEM dataset. (b) Virtual axial bright field image. (c) Virtual bright field image. (d) Virtual dark field image.

- [4] S. D. Findlay, Yuji Kohno, L. A. Cardamone, Yuichi Ikuhara, and Naoya Shibata. Enhanced light element imaging in atomic resolution scanning transmission electron microscopy. *Ultramicroscopy*, 136:31–41, 2014.
- [5] A. P. Pogany and P. S. Turner. Reciprocity in electron diffraction and microscopy. *Acta Crystallographica Section A: Crystal Physics Diffraction Theoretical and General Crystallography*, 24(1):103–109, 1968.
- [6] D. B. Williams and C. B. Carter. *Transmission electron microscopy: A textbook for materials science*. Springer, New York, NY, 2009.
- [7] Ivan Lazić, Eric G.T. Bosch, and Sorin Lazar. Phase contrast STEM for thin samples: Integrated differential phase contrast. *Ultramicroscopy*, 160:265–280, 2016.
- [8] Shoucong Ning, Wenhui Xu, Yinhang Ma, Leyi Loh, Timothy J. Pennycook, Wu Zhou, Fucai Zhang, Michel Bosman, Stephen J. Pennycook, Qian He, and N. Duane Loh. Accurate and robust calibration of the uniform affine transformation between scan-camera coordinates for atom-resolved in-focus 4D-STEM datasets. *Microscopy and Microanalysis*, 28(3):622–632, 2022.

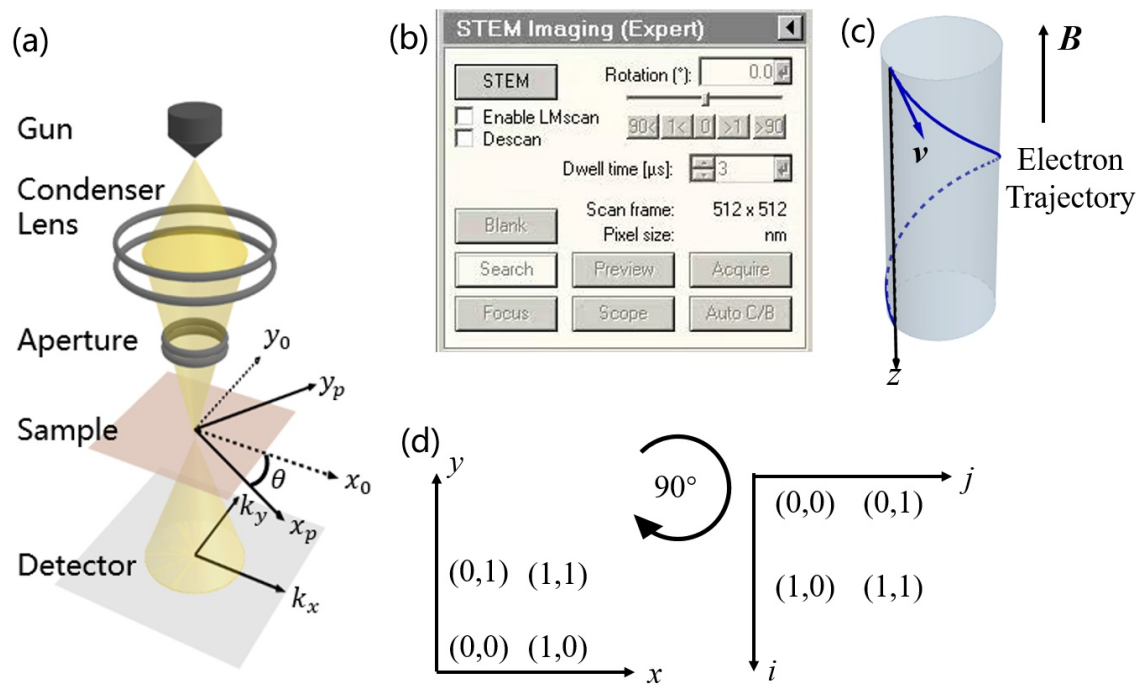


Figure S2: The source of rotational offset. (a) The schema of the rotational offset, inducing the rotational angle θ between the scanning coordinate and the diffraction coordinate. (b) Operation panel of TEM Imaging & Analysis (TIA). Users can manually set the scanning rotations during 4D-STEM experiments. (c) The helical trajectory of electrons caused by magnetic lenses. (d) Different choices of coordinate basis during computing. There exists a rotation of 90 degree between $x - y$ coordinates and $i - j$ indices.

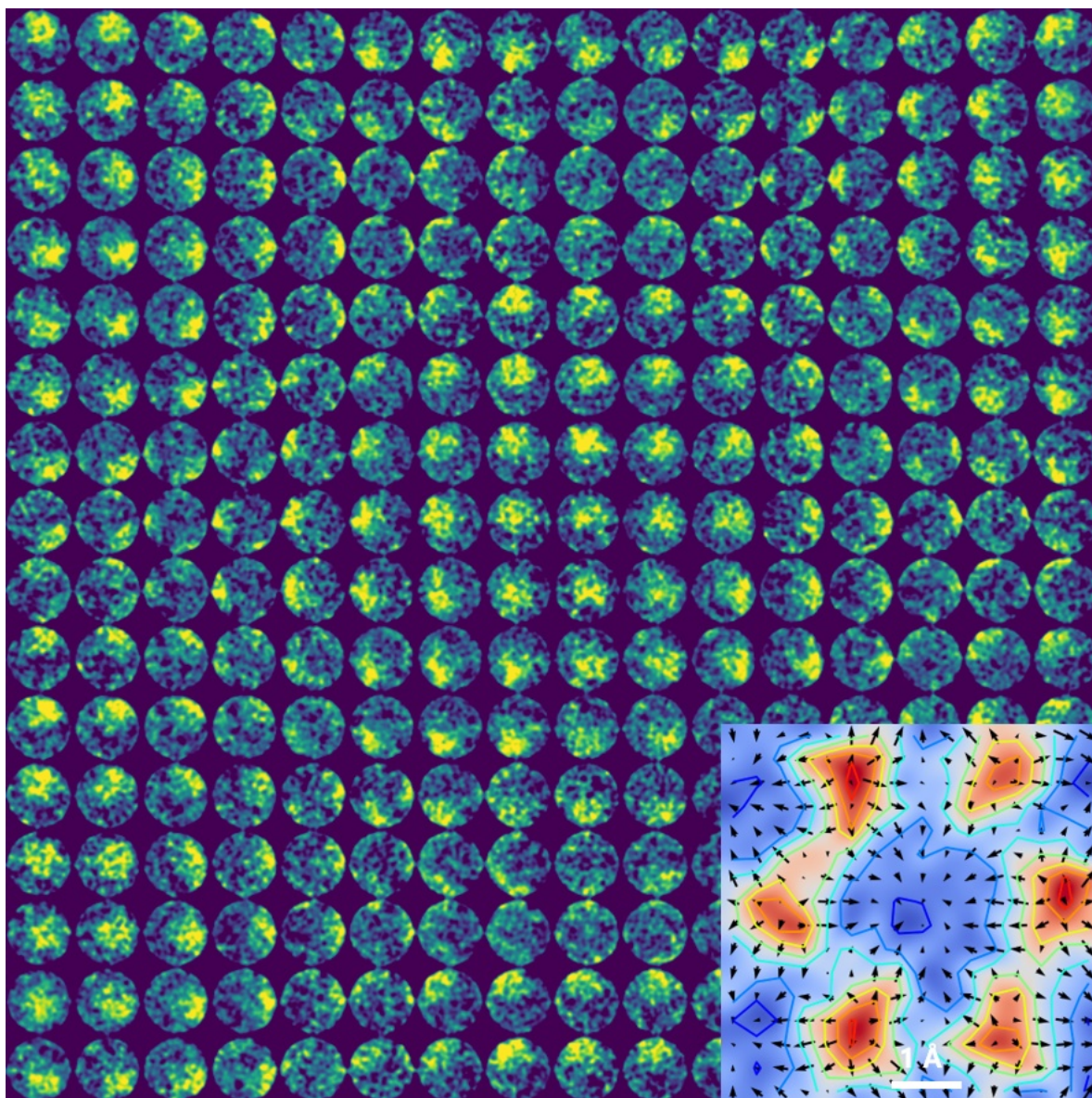


Figure S3: Diffraction Patterns of the MoS₂ dataset. The center of mass of the patterns are shifted due to electric fields around the atom columns.

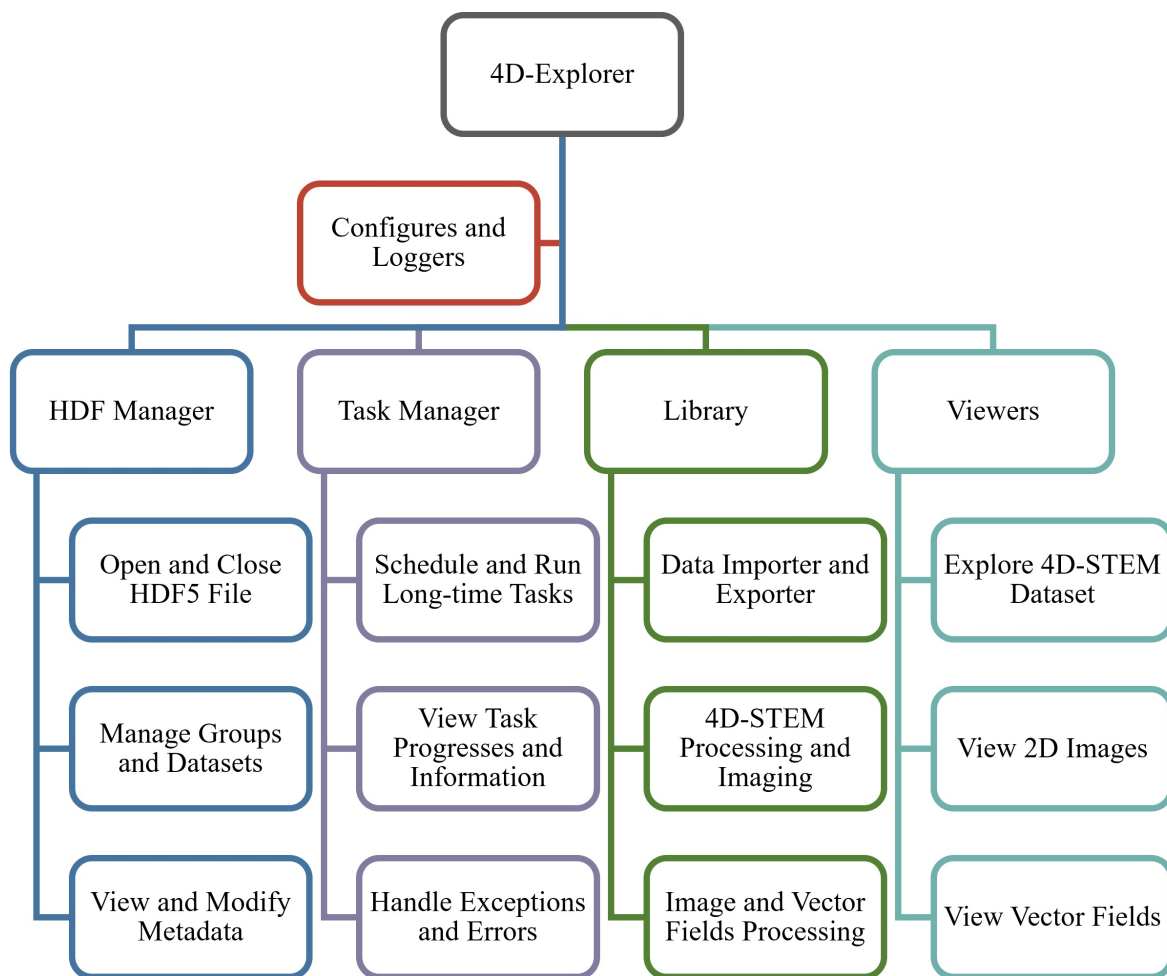


Figure S4: The architecture and key components of 4D-Explorer and their key features. The hierarchy file format (HDF) manager handles data storage and their IO. The task manager keeps an executor with a thread pool for concurrent tasks, and will run these tasks automatically in the background without blocking the user interface. The library contains functions and algorithms, and encapsulate them into tasks. The viewers are actually a collection of dedicated displaying pages for different purposes. Apart from these components that directly related to 4D-STEM processing, other miscellaneous modules also support the functionality of the software, like the configuration manager and the loggers.

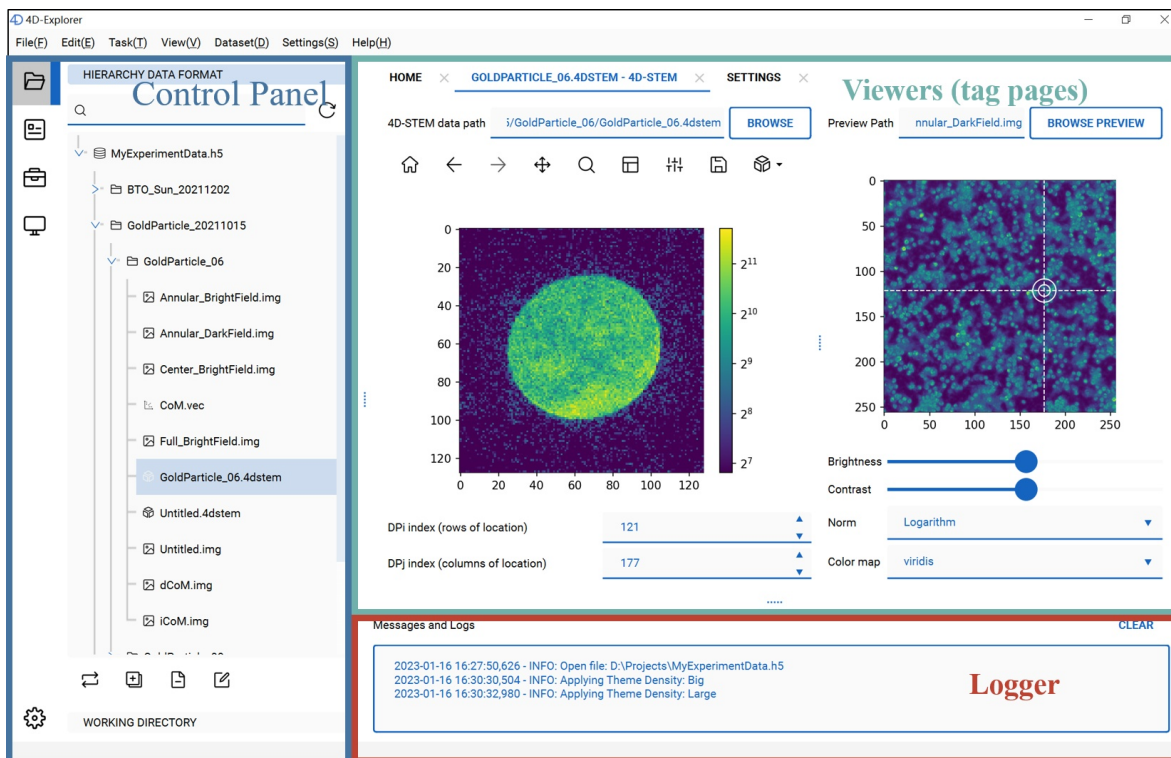


Figure S5: The 4D-Explorer Main window. The control panel, the 4D-STEM viewer and the logger are displayed.

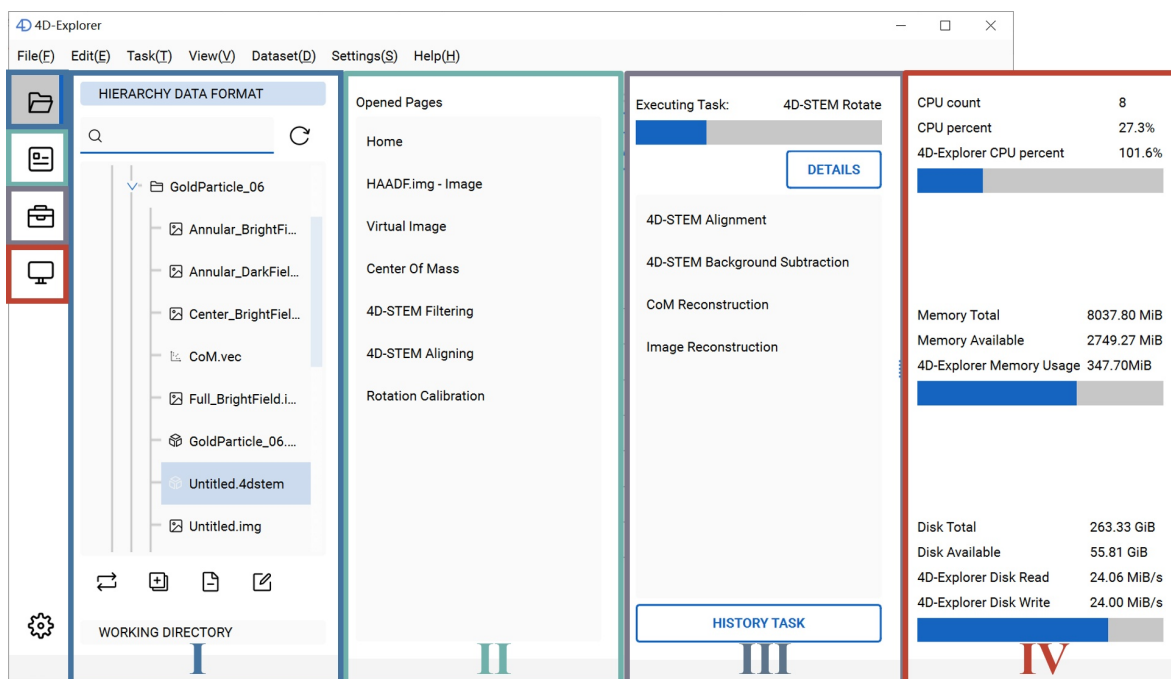


Figure S6: Control panel. **I** File manager. Groups and datasets inside are displayed. **II** Currently opened viewers (tag pages). **III** Task Manager. Different compute tasks are executed in background. **IV** System information.

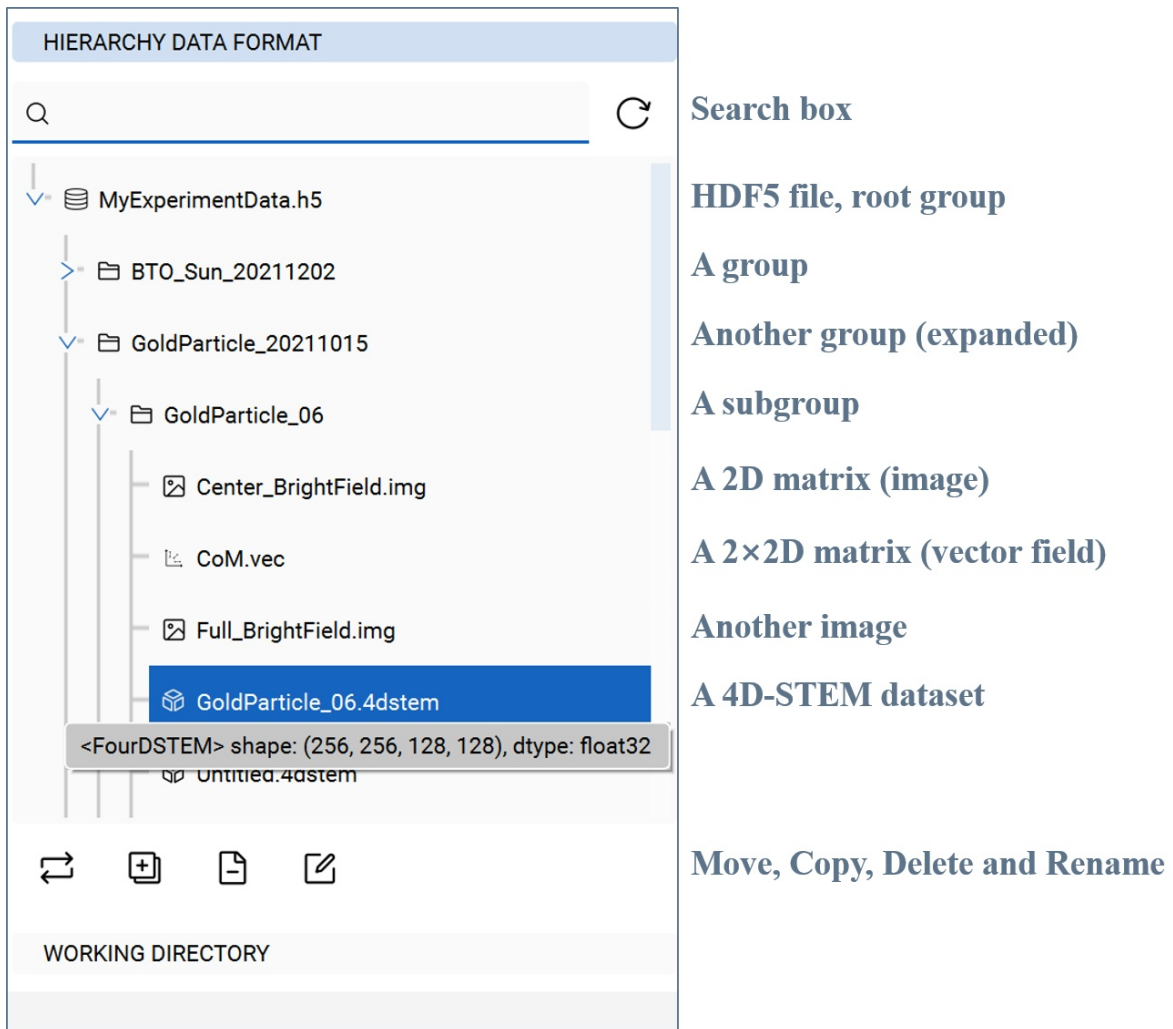


Figure S7: File manager. The groups and datasets are organized as a tree in an HDF5 file. The HDF5 file here is `MyExperimentData.h5`, and it is also the root group. Inside the file, there are several groups and subgroups. There are some datasets in a group `GoldParticle_06`, which have different sizes and usage hinted by the extensions. For example, `Center_BrightField.img` is a 2D matrix, can be viewed as an image, and has an extension `.img`. Extensions include `.vec`, `.4dstem` and so on.

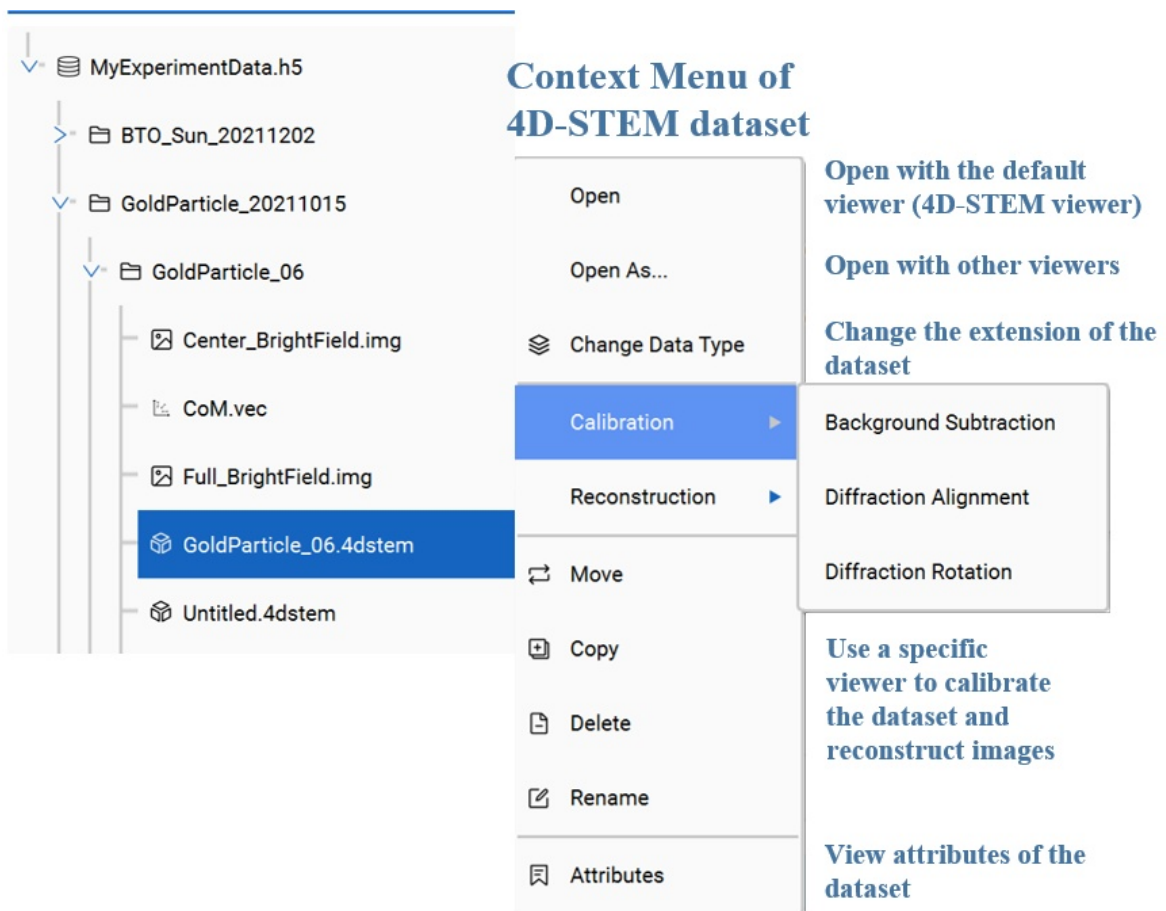


Figure S8: A 4D-STEM dataset and its available actions.

KEY	VALUE
acquire_datetime	2021-10-15T09:13:42.419274
camera	EMPAD
camera_length	0.5766
data_mode	4D-STEM
dp_i	128
dp_j	128
dp_pixel_size_i	0.0005376344086021505
dp_pixel_size_j	0.0005376344086021505
dp_pixel_size_unit	rad
empad_version	0.51 211118
filter_window_max	3163.24
filter_window_min	11.670000000000002
full_scan_field_of_view_i	4.1898856161226796e-07
full_scan_field_of_view_j	4.1898856161226796e-07
header_file	D:...
preview_path	/GoldParticle_20211015/...
raw_file	D:...
scan_i	256
scan_j	256
scan_rotation	0.5235987666666668
scan_size	0.55

The path of this dataset in the HDF5 file

- Acquisition time of raw data
- 4D-STEM camera
- Camera length (CL)
- Dataset type
- Diffraction pattern vertical size (in pixel)
- Diffraction pattern horizontal size (in pixel)
- Diffraction pattern pixel vertical size (in rad)
- Diffraction pattern pixel horizontal size (in rad)
- Diffraction pattern pixel size unit
- 4D-STEM camera software version
- Calibrating filter window of diffraction pattern (maximum value)
- Calibrating filter window of diffraction pattern (minimum value)
- Full vertical scanning field of view of companion STEM image (in m)
- Full horizontal scanning field of view of companion STEM image (in m)
- Header file path of the original experiment data
- Preview image path in the HDF5 file of this 4D-STEM dataset
- Raw file path of the original experiment data
- Scanning vertical pixel number
- Scanning horizontal pixel number
- Calibrated scanning rotation angle (in rad)

Figure S9: Attributes of the 4D-STEM dataset in Figure S8.

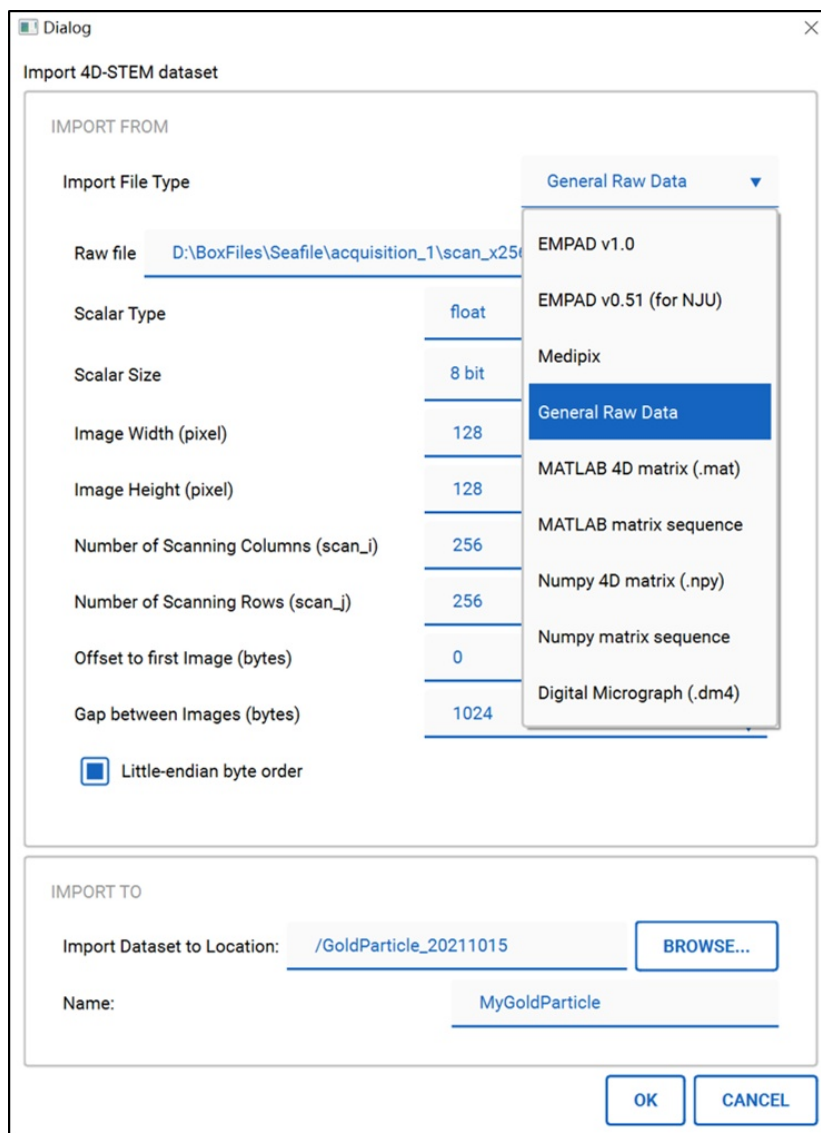


Figure S10: Import 4D-STEM datasets. For general binary file (raw data), the reading arguments such as data type, height, width and offset can be customized. There are also predefined importer shown in the combobox. Dataset stored in the HDF5 file can also be exported as these kinds of files in similar processes.

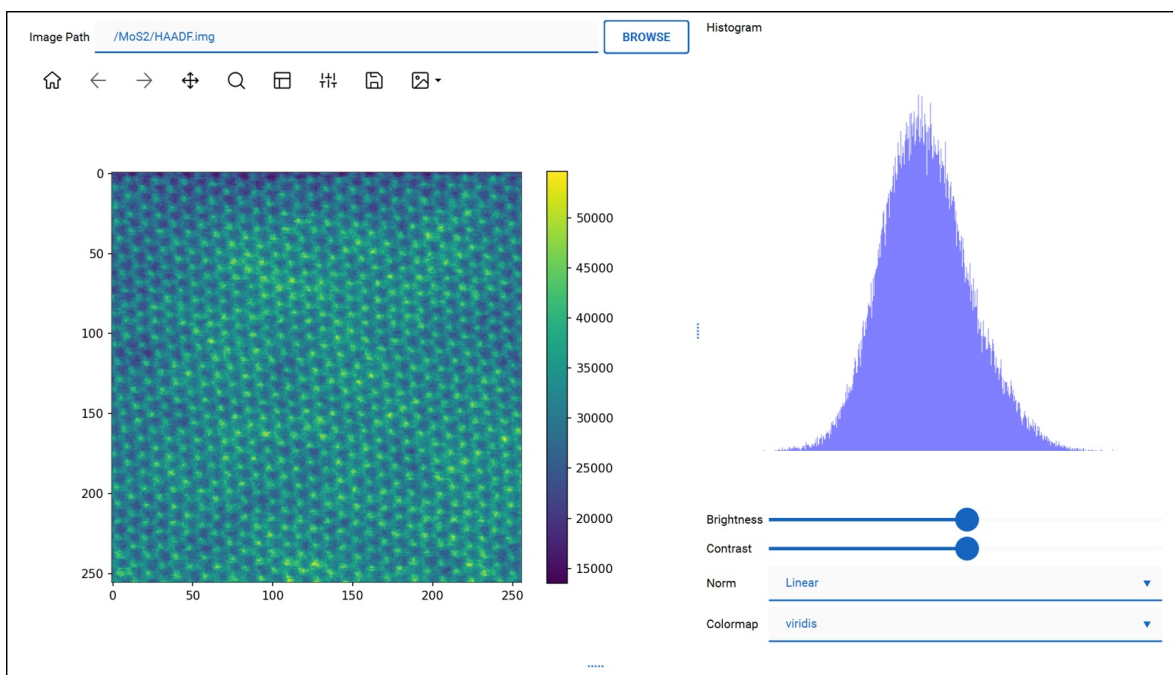


Figure S11: The image viewer.

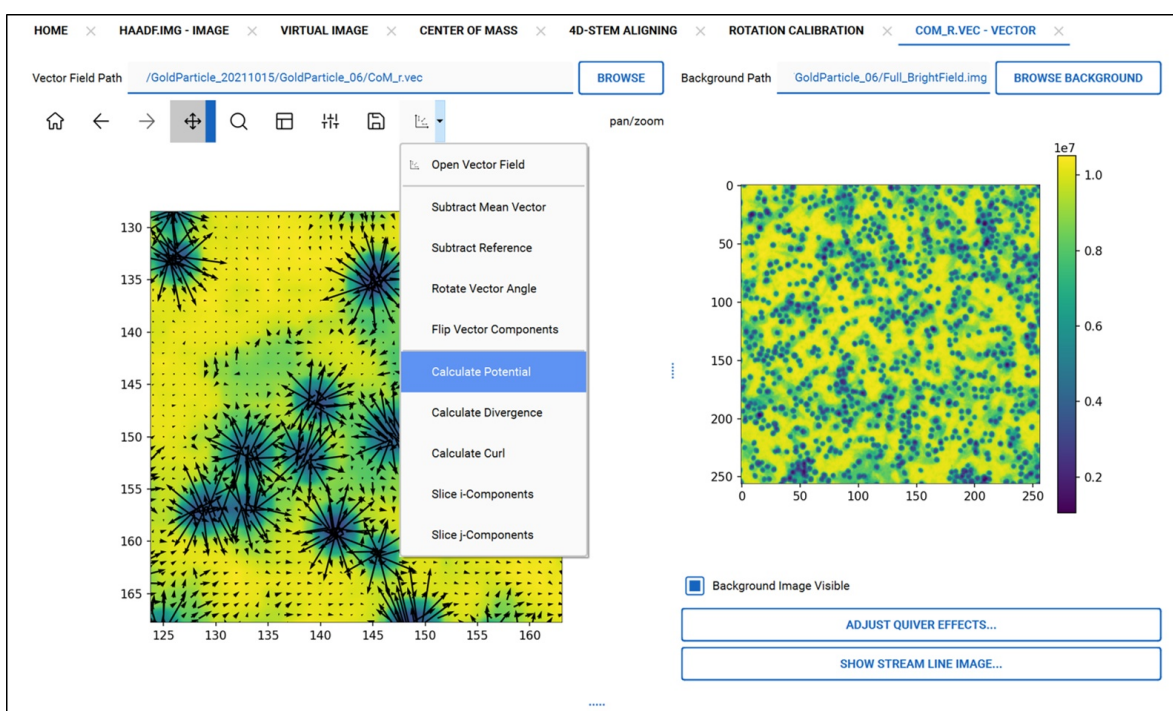


Figure S12: The vector field viewer. The opened combobox here shows available actions to a vector field dataset. For a CoM distribution, we can compute its potential, divergence and curl to acquire iCoM, dCoM and cCoM respectively.

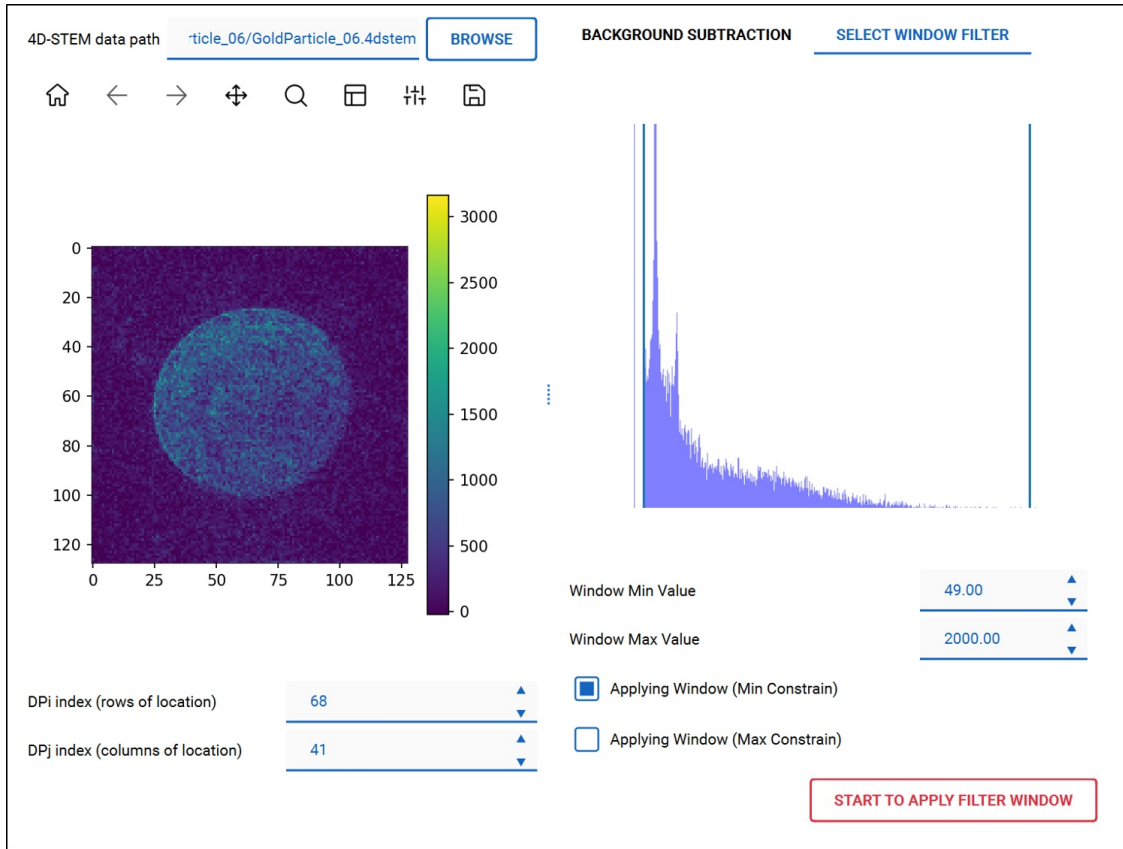


Figure S13: The background subtraction viewer. The two blue vertical lines in the histogram are the two edges of the window filter.

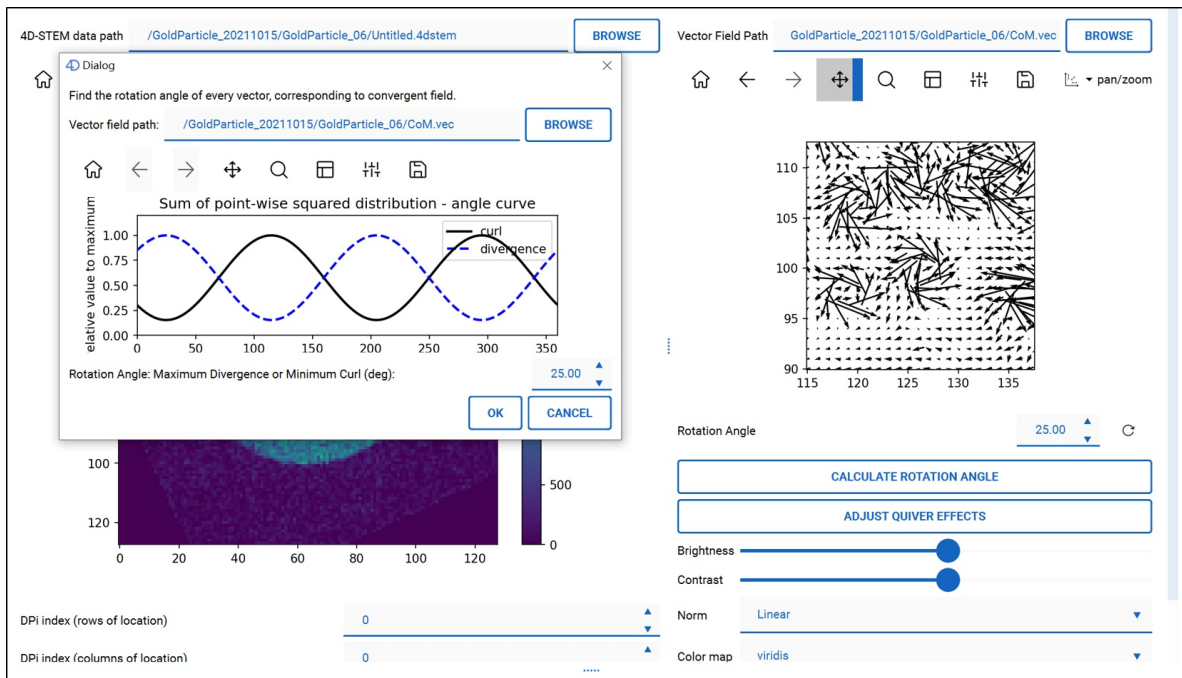


Figure S14: The rotational offset correction viewer. We can solve the rotational offset angle by minimizing the curl of CoM vector field.

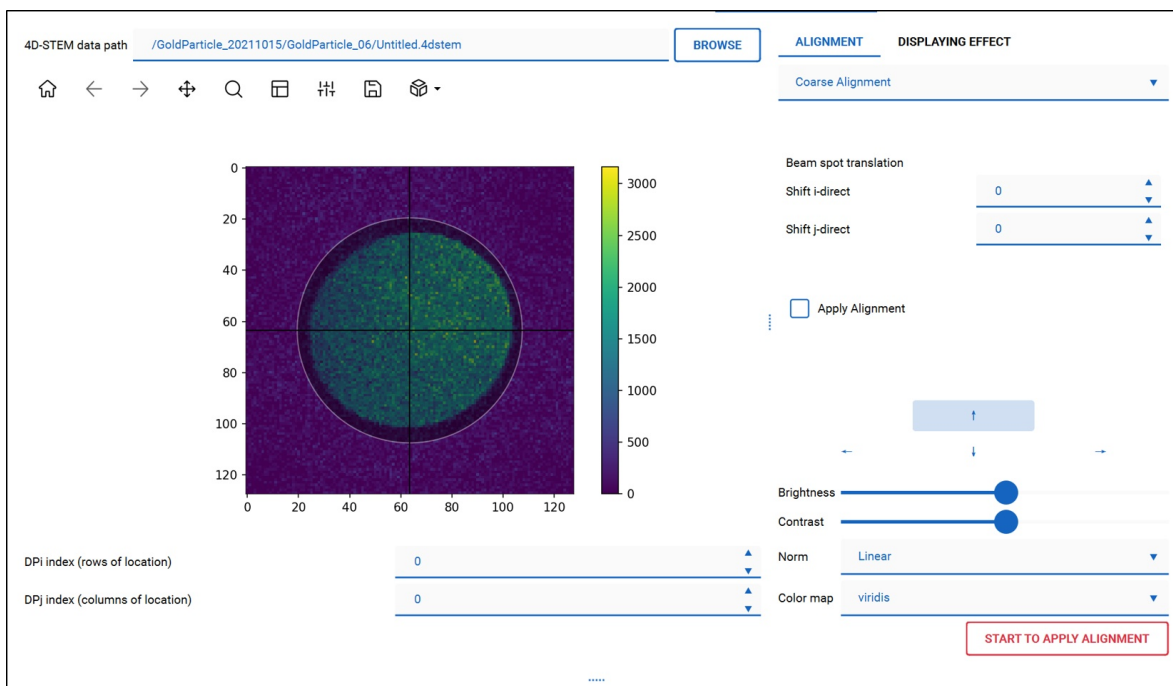


Figure S15: The diffraction alignment viewer.

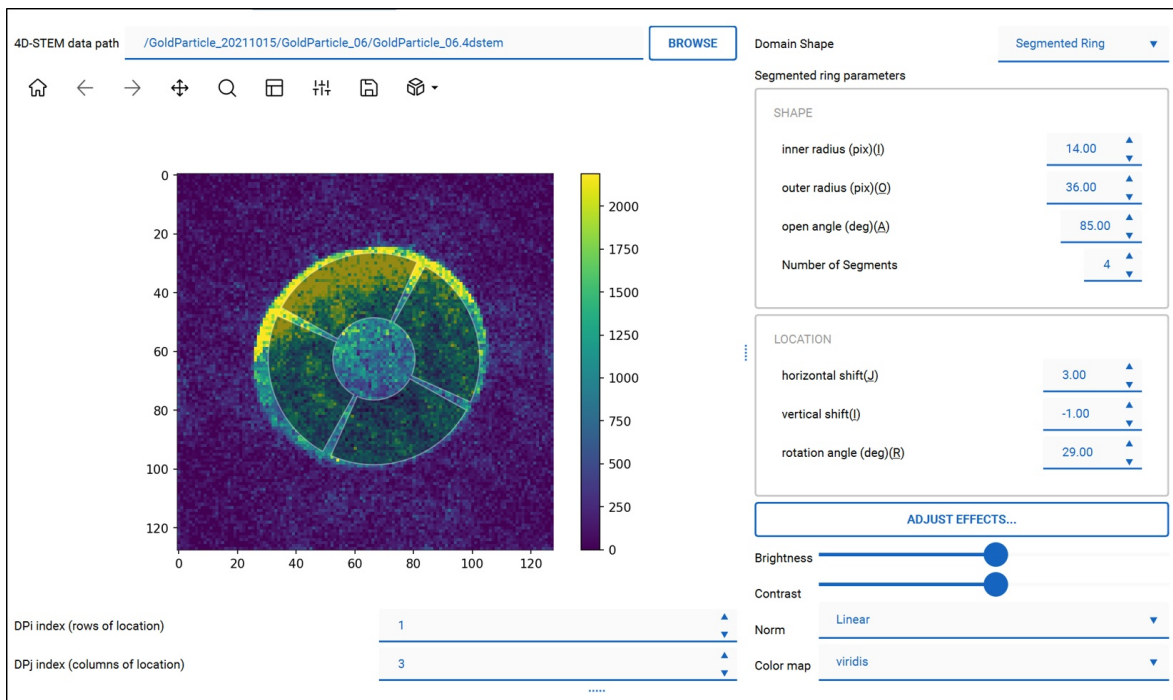


Figure S16: The virtual image viewer. 4D-Explorer supports many virtual detector shapes for different purposes, including annulus, ellipse, rectangle and segmented wedges.